Frequency Dependent Mantle Viscoelasticity via the Complex Viscosity: cases from Antarctica

H.C.P. Lau[1], J.A. Austermann[2], B.K. Holtzman[2], C. Havlin[3], A.J. Lloyd[2], C. Book[1], E. Hopper[2]

[1]Earth and Planetary Science, University of California, Berkeley, CA. USA
[2]Lamont-Doherty Earth Observatory, Columbia University, Palisades, NY. USA
[3]School of Information Sciences, University of Illinois, Urbana-Champaign, IL. USA

Key Points:

- Differing estimates of viscosity and plate thicknesses are observed from various loading processes across Antarctica
- Using new theory and laboratory laws, frequency dependent viscosity and plate thickness are predicted for Antarctic sites
- Our results indicate that these predictions of viscosity and plate thickness can significantly contribute to the observed discrepancies

Corresponding author: Harriet C.P. Lau, hcplau@berkeley.edu

Abstract

Studies of glacial isostatic adjustment (GIA) often use paleoshorelines and present-day deformation to constrain the viscosity of the mantle and the thickness of the elastic lithosphere. However, different studies focused on similar locations have resulted in different estimates of these physical properties. We argue that these different estimates infer apparent viscosities and apparent lithospheric elastic thicknesses, dependent on the timescale of deformation. We use recently derived relationships between these frequency dependent apparent quantities and the underlying thermodynamic conditions to produce predictions of mantle viscosity and lithospheric thickness across a broad spectrum of geophysical timescales for two Antarctic locations (Amundsen Sea and the Antarctic Peninsula). Our predictions are constrained by input from seismic tomography, require the self-consistent consideration of elastic, viscous, and transient rheological behavior and also include non-linear steady state viscosity, which have been determined by several laboratories. We demonstrate that these frequency dependent predictions of lithospheric thickness and apparent viscosity display a significant range and that they align to first order with estimates from GIA studies on different timescales. We suggest that observational studies could move towards a framework of determining the frequency dependence of apparent quantities – rather than single, frequency independent values of viscosity – to gain deeper insight into the rheological behavior of Earth.

Plain Language Summary

The viscoelastic structure of the solid Earth has important consequences for ice-melting events, and other processes that involve shifting mass on Earth's surface. As mass moves on Earth's surface, the Earth subsides or rebounds, where the degree and time-scale of these responses depend on Earth's viscosity. Inferences of Earth's viscosity often consider a single viscosity that does not take into account the time-scale effects of how slowly or quickly mass is exchanged on Earth's surface (e.g., ice sheet collapse compared with slow melt spanning thousands of years). Using a new theoretical framework and applying it to cases in Antarctica (in particular, the Antarctic Peninsula and Amundsen Sea Embayment), we demonstrate that such time-scale factors should be considered for future studies.

1 Introduction

The growth and decay of ice sheets over the Pleistocene represent large variations in Earth's climate system and induce significant deformation of the solid Earth. This deformation (including associated changes to Earth's gravity field and rotation), in response to the redistribution of ice and ocean mass, is known as "glacial isostatic adjustment" (GIA). Areas that were formerly covered by or close to major ice sheets during the last glacial period, such as North America and Antarctica, continue to experience the highest rates of GIA-related deformation, even though ice has retreated partially or entirely (e.g., Sella et al., 2007). Pertinent to understanding this solid Earth deformation, and, as a consequence, related climatological feedbacks (e.g., Larour et al., 2019; Pan et al., 2021) is knowledge of the planet's viscoelastic structure.

Constraining Earth's viscoelastic structure has been the focus of many GIA, geodynamic, seismic, and mineral/rock physics studies. In GIA studies, viscoelastic deformation is often assumed to be linear with one viscous timescale (Maxwell rheology), linear with multiple viscous timescales (transient, e.g., Burger's rheology), or a combination of linear and non-linear deformation (e.g., composite rheology)(see Fig. 2). This means that deformation can be timescale- or stress-dependent. In all cases, viscosity is additionally dependent on the thermodynamic state variables (most importantly temperature, but also composition, grain size, melt fraction, or water content), which causes it

to vary radially and laterally within the mantle (e.g. Kaufmann et al., 2005; Hay et al., 2017; Nield et al., 2018; Powell et al., 2020).

Transient behavior in form of a Burger's rheology has been considered in some GIA studies (e.g., Caron et al., 2017) in which observations are used to constrain the two distinct viscosities (Fig. 2). In addition, comparisons between model predictions including steady-state non-linear mechanical effects and observations of deglacial sea level have also been explored in GIA (e.g., Wu, 1992; van der Wal et al., 2010, 2013; Huang et al., 2019). In this study we aim to investigate the role of more complex rheologies by simultaneously exploring the effects of frequency dependent and non-linear rheology on GIA in Antarctica.

We use a new theoretical framework (Lau & Holtzman, 2019) to predict continuous frequency- and stress-dependent rheological parameters relevant for GIA for two regions beneath Antarctica: Amundsen Sea Embayment "ASE" and the Antarctic Peninsula "AP", Fig. 1(C). The upper mantle of two locations have been recently constrained by seismic structural models (Lloyd et al., 2019; An et al., 2015) and each location has experienced a variety of ice melt processes that span a range of timescales readily available to compare to our forward predictions. Additionally, because these are locations of rapid present-day ice melt at which GIA might help to stabilize the ice sheet, understanding the rheology is of particular importance. Lastly, focusing on distinct locations rather than larger regions allows us to minimize – to some extent – the effect of lateral variability in viscoelastic structure on the observed GIA response.

The variation of GIA responses to the wide variety of mass perturbations is well studied (e.g., Haskell, 1935; Peltier & Andrews, 1976; Nakada & Lambeck, 1989; Spada, 2017; Whitehouse, 2018) and analyses are often cast in terms of two controlling Earth parameters: mantle viscosity and the elastic thickness of the lithosphere, z_{LAB}. We will hone in on mantle viscosity down to 400 km depth, which we refer to as the "uppermost upper mantle", i.e., η_{UMM}. Fig. 1(A,B) displays estimates of these two parameters from regionally overlapping geophysical studies that observed GIA responses to, e.g., recent rapid ice sheet collapses (Barletta et al., 2018) and deglacial ice melt (Wolstencroft et al., 2015) (see caption for all references). Since our aim is to understand frequency dependent behaviour, we broadly subdivide these inferences into the timescale of observations from which they were derived (shorter centennial and longer millennial timescale loading processes "short" and "long", and, for z_{LAB} estimates, seismic structural models). We note that, at short timescales, accurate knowledge of viscoelastic properties is important for predicting the rebound process, with important implications for future ice and sea level change (Barletta et al., 2018; Pan et al., 2021).

Figs 1(A,B) reveal inconsistencies between the inferred values for these parameters for each site. While the differences between the two sites may be explained by varying thermodynamic state, the different measurements should in principle agree between each other at the same site. This apparent discrepancy can arise from two main sources: (i) differences in what depth and lateral range of viscosity these processes sample (van der Wal et al., 2015; Crawford et al., 2018); and (ii) differences in the nature – more specifically, the stress and time dependence – of the GIA response to mass perturbations. In this study, we do not aim to uniquely resolve these apparent discrepancies. Instead, we provide an in-depth investigation of (ii), to appreciate the extent to which these processes *could* contribute to the apparent discrepancy in the inferred viscoelastic structure.

The frequency dependent behavior of viscosity has long been demonstrated within experimental studies of the mechanical behavior of rock: The endmember elastic (and anharmonic) and viscous properties of rock have been well characterized in the experimental and theoretical rock physics community (e.g., Stixrude & Lithgow-Bertelloni, 2005; Hirth & Kohlstedt, 2003). In between these endmembers is the anelastic or transient regime, which is currently being explored by several laboratories working on olivine

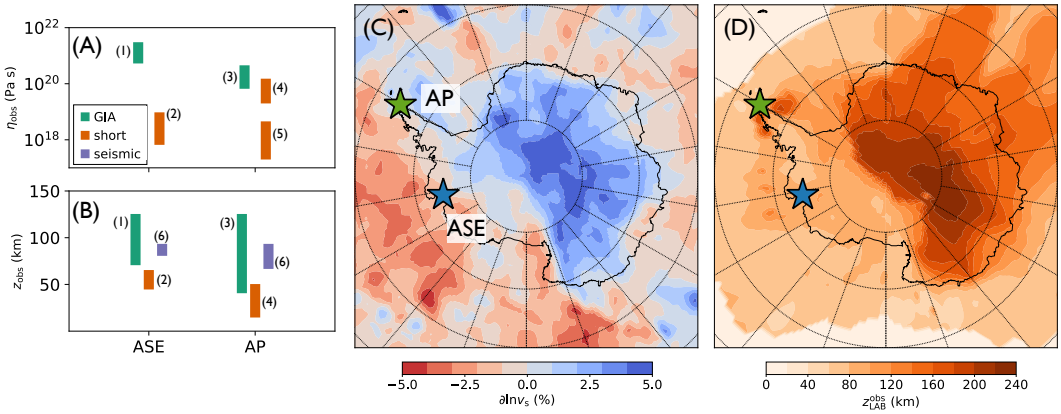

Figure 1. Estimates and locations of upper mantle viscosity and plate thickness. A compilation of (A) upper mantle viscosity, η_{obs}, and (B) lithospheric thickness, z_{obs}, estimates across the Amundsen Sea Embayment (ASE) and the Antarctic Peninsula (AP). References labeled are (1) Whitehouse et al. (2012); (2) Barletta et al. (2018); (3) Wolstencroft et al. (2015); (4) Ivins et al. (2011); (5) Samrat et al. (2020); and (6) An et al. (2015). (C) The seismic tomography model of Lloyd et al. (2019) at 225 km depth. Locations of ASE (102.667 °W; 64.833 °S); and AP (60.409 °W; 64.476 °S) are marked. (D) The seismically derived estimates of lithospheric thickness from An et al. (2015). Note, the lithospheric thickness estimates are based on the tomography model of An et al. (2015) and thus are not necessarily in agreement with ANT-20 (Lloyd et al., 2019).

samples (e.g., Jackson & Faul, 2010; Sundberg & Cooper, 2010; Faul & Jackson, 2015) and analogue materials (Takei, 2017). This work is building towards a clearer picture of the grain-scale processes that govern macroscopic transient creep, including both diffusion- and dislocation- (both linear and non-linear) related grain boundary and intracrystalling deformation mechanisms (e.g., Karato & Wu, 1993; Hansen et al., 2019). (See Havlin et al. (2021) for a summary of these processes.) From these microphysical mechanisms, distinct frequency-dependent rheological properties of rock can be predicted.

The broad goal of this study is to quantify and test the role of frequency and stress-dependent viscoelastic deformation in the two specific study regions (Fig. 1). In Section 2 we briefly summarize relevant experimental and theoretical background and present the framework introduced by Lau and Holtzman (2019) which will serve as a basis for our interpretation. These constitutive laws require thermodynamic conditions as input, and we use seismic observations to constrain this (Section 3). With the thermodynamic conditions of each region determined, we predict their complex viscosities, $\eta^*(\omega; z)$ (which is a measure of viscous dissipation, introduced in Section 2), spanning geophysically relevant frequencies. With this approach we treat viscoelastic rheology in a manner akin to mapping attenuation as a function of frequency, $Q^{-1}(\omega)$, as studied within the fields of seismology and Earth tides (Shito et al., 2004; Benjamin et al., 2006; Lekić et al., 2009; Lau & Faul, 2019). In order to compare our $\eta^*(\omega)$ predictions to results from prior GIA studies we first determine the frequency content of the time-domain GIA data (Fig. 1) and then investigate to what extent the predicted values of both η_{UMM} and z_{LAB} as a function of frequency can contribute to the variation obtained in the observationally driven estimates.

2 The full spectrum of viscoelastic deformation

In the following we first describe phenomenological models that are typically used to describe viscoelastic behavior noting where each regime of deformation lies in relation to these models (Section 2.1). We then follow with how we can use the complex viscosity to derive two frequency dependent parameters relevant to GIA dynamics, the apparent viscosity and lithospheric thickness (Section 3.1.3). This ultimately requires knowledge of the mechanical properties of rock across all frequencies of interest (hereafter, the "full spectrum" mechanical properties).

To do this we will rely on a recently released open-source software library, the "Very Broadband Rheology calculator" (VBRc), developed by several of the co-authors here (Havlin et al., 2021). This software takes as input the thermodynamic conditions and other state variables, $\mathcal{S}$ – where $\mathcal{S} = [T, P, \phi, g, \sigma, X]$ (temperature, pressure, melt fraction, grain size, stress state, and composition, respectively) – and determines the full spectrum mechanical properties for a selection of constitutive laws. In Section 2.3 we briefly describe this process.

In Section 2.4 we describe our current understanding on the broadband characteristics of deformation from the experimental community and how these micro-scale descriptions are applied to geophysical applications. We subdivide these into their deformational regimes (elastic, viscous, transient, and non-linear) and also describe the specific constitutive laws the VBRc implements for each.

2.1 Summary of Phenomenological Models

In order to incorporate frequency-dependent properties predicted by experiments into geophysical forward predictions, the constitutive laws are described by phenomenological parameterizations via combinations of springs (described by modulus M_i) and viscous dashpots (described by viscosity η_i) that, in isolation, characterize elastic and viscous behavior, respectively. The simplest arrangement is a single spring-dashpot pair in series, known as the Maxwell model (see Fig. 2). This is the most common viscoelastic model considered in GIA studies since a convenient semi-analytical solution may be determined (e.g., Peltier & Andrews, 1976; Nakada & Lambeck, 1989; Mitrovica & Milne, 2003).

Fig. 2 partitions the different flavors of phenomenological models in their different frequency limits. All models have two endmembers in common: The elastic regime occurs at infinite frequency ($f \rightarrow \infty$) where no energy is dissipated and deformation is both instantaneous and fully recoverable. Any quantity corresponding to this endmember, e.g., the modulus, M, will be specified as M_∞. The opposite endmember refers to the viscous or steady-state regime, when $f \rightarrow 0$, wherein deformation is fully dissipative and no longer recoverable. Quantities, like M, associated with this frequency limit will be denoted M_0.

In between these endmembers, there exists the transient creep regime. Within transient creep, anelastic processes may occur, where deformation is fully recoverable, though time dependent. Such behavior may be mimicked by Kelvin-Voigt pairs (one spring and one dashpot in parallel). Such recovery reflects microscopic restoring forces (Section 2.4.3). However, irrevserible material transport also accompanies transient creep. (If transient creep does indeed occur during GIA, gravity provides a macroscopic restoring force, analogous to elasticity at the grain scale) Additional transient elements can be added to the Maxwell model to account for anelastic effects, giving rise to more complex models such as the Andrade model (Sundberg & Cooper, 2010), the Extended Burgers model (Faul & Jackson, 2015), and relaxation function fitting approaches (McCarthy et al., 2011; Yamauchi & Takei, 2016). In addition, complexity can arise from non-linear (stress-dependent) effects (Hirth & Kohlstedt, 2003; Hansen et al., 2011).

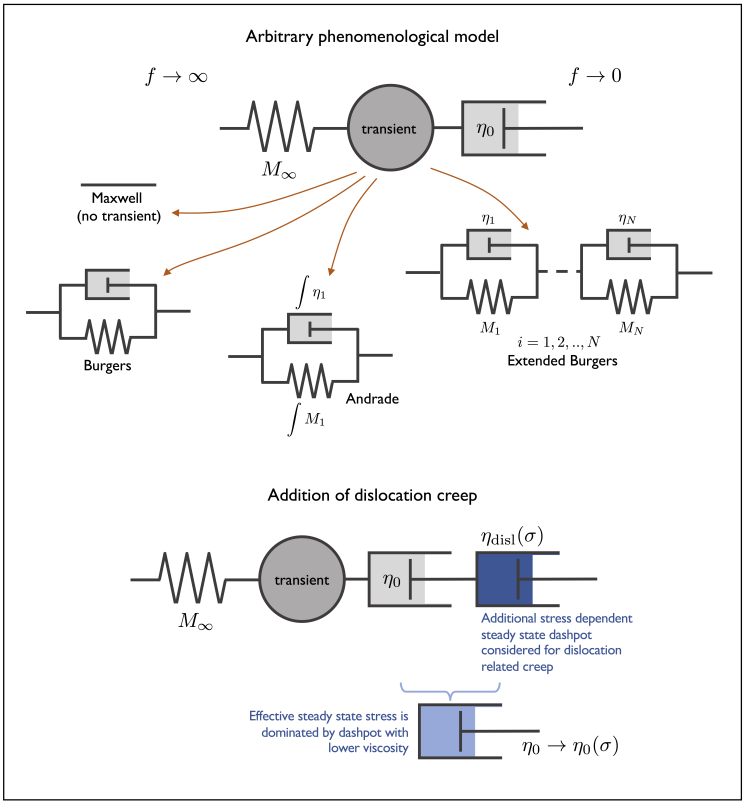

Figure 2. Phenomenological Viscoelastic Models. Depiction of 1-D phenomenological viscoelastic models. The dark gray circle symbolically represents any combination of springs and dashpots that mimic transient deformation. Replacing the circle with any of the components linked by an arrow will form the commonly adopted models labelled. With the addition of steady state dislocation creep, the viscosity of the steady state dashpot, η_0, becomes stress, σ, dependent.

From these phenomenological models several measures of dissipation may be determined depending on the arrangement of the discrete springs, M_i, and dashpots, η_i, including the dissipation (or attenuation), $Q^{-1}(\omega)$, the complex modulus, $M^*(\omega)$, and its inverse, the complex compliance, $J^*(\omega)$. The latter two have their time-domain equivalents, $M(t)$ and $J(t)$ (Nowick & Berry, 1972). The latter is known as the creep function. We will also introduce the complex viscosity, $\eta^*(\omega)$, which is distinct from the discrete dashpots within any given phenomenological model.

2.2 Complex Viscosity

Lau and Holtzman (2019) explored the use of complex viscosity, $\eta^*(\omega)$, in geophysical applications involving viscoelasticity, building on its use more commonly within the materials science literature (e.g., Gunasekaran & Ak, 2002). To motivate its application, we begin with the more familiar (and closely related) complex modulus, $M^*(\omega)$. $\mathrm{Re}[M^*(\omega)]$ reduces with decreasing frequency, causing the dispersion of seismic waves, while $\mathrm{Im}[M^*(\omega)]$ captures the dissipative effects. Within seismology, dispersion manifests as the reduction of seismic wave-speeds at lower frequencies (e.g., Kanamori & Anderson, 1977). Similarly, attenuation, Q^{-1}, where

$$Q^{-1}(\omega) \equiv \mathrm{Im}[M^*(\omega)]/\mathrm{Re}[M^*(\omega)], \tag{1}$$

increases with lower frequency across the seismic band (e.g., Shito et al., 2004; Lekić et al., 2009) and the tidal band (Benjamin et al., 2006; Lau & Holtzman, 2019). In Fig. 3(A) we show a schematic figure of how these parameters are sampled by seismic waves of different frequency. *No specific phenomenological model* is assumed, only the measurements of $Q^{-1}(\omega)$ and $v(\omega)$ at their given frequency are determined, such that a frequency trend may be mapped out.

Lau and Holtzman (2019) extended this analogy to GIA by using a more appropriate parameter, $\eta^*(\omega)$. The relationship between $\eta^*(\omega)$ and $M^*(\omega)$ is

$$\eta^*(\omega) = i\frac{M^*(\omega)}{\omega} \tag{2}$$

and upon inspection, one can see that η^* has the same units as viscosity, where the real and imaginary parts, and their physical meaning, have now been switched relative to M^*. No matter the arrangement of springs and dashpots, analagous to $M^*(\omega)$, a continuous function of $\eta^*(\omega)$ across frequency may be derived.

Just as the dispersion of wave-speed captures $\mathrm{Re}[M(\omega)]$ (or more specifically, its square-root), we argue that estimated viscosities determined by different observations are sampling $\|\eta^*(\omega)\|$ at their respective frequency bands (Fig. 3B), where we have plotted $\|\eta^*(\omega)\|$, the *apparent* viscosity (Section 3.1.3) of a Maxwell viscoelastic model. For clarification, while the Maxwell model has a single viscous dashpot, since it also has a frequency dependent complex modulus, eq. 2 shows that even the Maxwell model will have a frequency dependent $\eta^*(\omega)$. The quantity $\|\eta^*(\omega)\|$ may be interpreted as an indication of the degree of viscous dissipation at a given frequency (Lau & Holtzman, 2019). By considering GIA inferred $\eta^*(\omega)$ at a given frequency of observation, the link to laboratory-based constitutive laws is clear. In contrast, discrete springs and dashpots obscure this connection.

2.3 The Very Broadband Rheology calculator (VBRc)

The Very Broadband Rheology Calculator (VBRc) is an open source software package recently developed by Havlin et al. (2021, available at https://vbr-calc.github.io/vbr/). Given a set of thermodynamic state variables, $\mathcal{S}$, it will predict the full spectrum mechanical properties for composition, X, of olivine (90% forsterite) assuming certain constitutive laws. By "full spectrum", we mean the elastic, anelastic, and viscous regimes

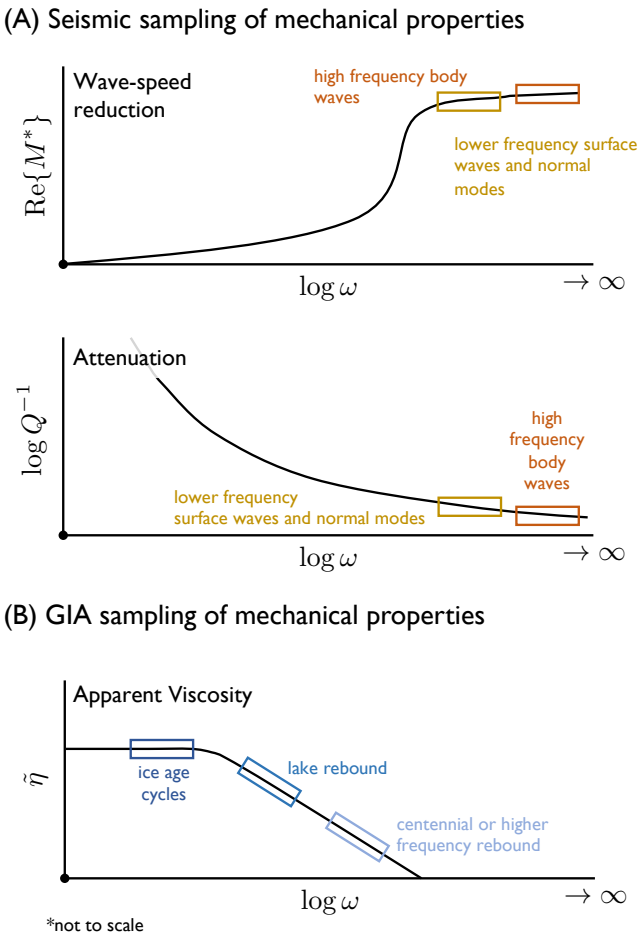

Figure 3. Mapping out dissipation parameters with geophysical observations. (A) A schematic depiction of seismic wave-speed reduction (top panel) with lowering frequency due to dispersion (or Re$[M^*(\omega)]$) and the increase of attenuation, $Q^{-1}(\omega)$ (bottom panel). Boxes denote how these trends are sampled by seismic data at different frequencies. (B) The analog to (A) but how GIA processes may sample apparent viscosity $\tilde{\eta}(\omega)$. Note, "lake rebound" refers to how the drainage of lakes can produce isosatic adjustment (e.g., the rapid drainage of Lake Bonneville (∼14 ky BP) over ∼500 y; Austermann et al., 2020).

of deformation. To tie these regimes together, $\mathcal{S}$ is used to determine the two endmember mechanical properties, i.e., the elastic and viscous endmembers. The anelastic regime is oftentimes scaled by the two endmember behaviors and is thus calculated after the unrelaxed modulus (M_∞, elastic endmember) and steady state viscosity (η_0) have been determined. The VBRc then outputs the complex modulus, $M^*(\omega)$, the dissipation, $Q^{-1}(\omega)$, from which the complex viscosity $\eta^*(\omega)$ (Lau & Holtzman, 2019) can be computed (Section 2.2). In the initial release of the VBRc, the composition is limited to olivine and the laboratory-derived rheological laws remain the focus (Havlin et al., 2021).

The experiments used to determine the constitutive laws in Section 2.4 only span a small thermodynamic range in comparison to deformational processes ocurring in Earth's mantle. Moreover, the timescales that we explore in this paper well exceed the typical experimental timescales. The basis for scaling experimental to mantle timescales is that the grain size (and/or subgrain size) is the primary controlling length scale for transient and steady state diffusion creep; finer grain sizes, as is the case for laboratory samples, enhance the kinetics such that appropriate strains can be achieved on practical timescales. While this approach is robust for steady state diffusion creep, many open questions remain on the scaling for transient diffusion creep and interactions with dislocation processes, discussed in (e.g. Cooper, 2002; Faul & Jackson, 2015; Takei, 2017; Havlin et al., 2021).

With this in mind, we use the VBRc to determine the full spectrum mechanical properties of the uppermost 400 km of the mantle from convection to seismic timescales in a continuous manner across the elastic, anelastic, and viscous regimes of deformation. By testing these extrapolations to real Earth observations across wide timescales, we may illuminate features of the scalings that are in need of revisiting.

2.4 The Frequency Dependence of Rheology

2.4.1 Elastic Endmember

There exists a wealth of work in constraining the elastic and density properties of a range of hypothesized bulk compositions and equilibrium mineral assemblages under P-T conditions across the mantle (e.g. Duffy & Anderson, 1989; Goes & van der Lee, 2002; Cammarano et al., 2003; Stixrude & Lithgow-Bertelloni, 2005; Khan et al., 2009). As discussed in Havlin et al. (2021), the focus of much of this literature is on thermally and compositionally driven variations in both shear and compressional wave speeds, v_s and v_p.

Within the elastic regime, two processes are at play: (1) Anharmonic effects within the lattice structure that cause elastic moduli, M_∞, to have a P-T-X dependence (Kumazawa & Anderson, 1969; Stixrude, 2007). Within the VBRc, the following dependence is adopted,

$$M_\infty(T,P) = M_\infty(T_\mathrm{R},P_\mathrm{R}) + (T-T_\mathrm{R})\frac{\partial M}{\partial T} + (P-P_0)\frac{\partial M}{\partial P}, \tag{3}$$

where the subscript "R" denotes the reference values, adopting derivatives and reference values of Isaak (1992). (2) Poroelastic effects that concern fluid inclusions and their mobility within a given matrix (e.g., O'Connell & Budiansky, 1977; Hammond & Humphreys, 2000) are accounted for using the contiguity model of Takei (1998) (assuming isotropy described in Appendix A of Takei (2002) with a constant fluid pressure). In total, the unrelaxed (or infinite frequency) modulus undergoes the following stages: we begin with $M_\infty(T_\mathrm{R},P_\mathrm{R})$ of bulk composition X, then apply anharmonic scalings to provide $M_\infty(P,T)$ and finally the poroelastic effect is included with the melt fraction, ϕ, and we point the reader to Takei (1998, 2002) for details.

2.4.2 Viscous Endmember

The steady state or viscous endmember is described by flow laws. Such laws have been developed based on creep experiments on San Carlos olivine samples by Hirth and Kohlstedt (2003) and Hansen et al. (2011). The former included diffusion and dislocation creep for both dry and "wet" olivine, where the latter expanded the dry laws to include dislocation-accommodated grain boundary sliding. The VBRc assumes that the deformation mechanisms operate in kinetic parallel (mechanical series), in which case the total strain rate, $\dot{\varepsilon}$, is given by the sum of the contribution for each mechanism:

$$\begin{aligned} \dot{\varepsilon}(\sigma, g, T) &= \sum_i \dot{\varepsilon}_i(\sigma, g, T) \\ &= \sum_i C_i \sigma_i^n g^{-m_i} \exp\left(-\frac{Q_i + PV_i^*}{RT}\right) \end{aligned} \tag{4}$$

where i = [diffusion creep, dislocation creep, dislocation-accommodated grain boundary sliding creep], Q_i is the thermal activation energy, and V^* is the activation volume. Thus, the steady state viscosity, η_0, for each mechanism may be found by $\eta_{0,i} = \sigma/\dot{\varepsilon}_i$ and the total effective steady state viscosity, η_0, is $\sigma/\dot{\varepsilon}$. In the VBRc, the values of Q_i, n_i, m_i, V_i^*, are provided from Hirth and Kohlstedt (2003) and Hansen et al. (2011). In the present study, we use the flow law described in the former.

Unless specified otherwise, we will focus on steady state diffusion creep, for which the stress exponent, n, in eq. 4 is 0. In Section 2.4.4 we will provide brief background on nonlinear ($n \neq 0$) effects on the steady state viscosity and will explore this effect further in Section 4.2.1.

2.4.3 Transient Creep and Anelasticity

Transient diffusion creep arises from stress concentrations at grain edges, driving diffusive flow of matter through grain boundaries or sub-grain boundaries, causing stress concentrations to relax (e.g. Cooper, 2002). This process is considered to cause the so-called "High Temperature Background" (HTB) attenuation in olivine (Gribb & Cooper, 1998; Cooper, 2002; Jackson & Faul, 2010). For example, as a seismic wave passes, small displacement on near inviscid grain boundaries produce stress concentrations at grain edges and faces (Raj & Ashby, 1971; Raj, 1975; Morris & Jackson, 2009). Such a process predicts a mild frequency dependence of dissipation or attenuation, Q^{-1}, where $Q^{-1}(\omega) \sim (\omega^{-\frac{1}{4}}$ to $\omega^{-\frac{1}{3}})$, well fit by the empirical Andrade model (Andrade, 1910), and demonstrated theoretically by Raj (1975); Gribb and Cooper (1998); Morris and Jackson (2009). Such a frequency dependence is not captured by the phenomenology of the Maxwell viscoelastic model (Fig. 2), as adopted by many GIA calculations which do not consider the possibility of activating such processes. It is also possible that the response of material undergoing this physics has an inherent similitude such that it may be scaled by the so-called Maxwell frequency, $f_{\mathrm{M}} \equiv M_\infty/\eta_0$, where mechanical parameters collapse onto a single curve when normalized by f_{M} (Cooper, 2002; McCarthy et al., 2011). The appropriate length scale (sub-grain, or grain) that is the most appropriate for scaling, and the related parameter values, are still under debate. We refer the reader to Havlin et al. (2021) for further discussion on these issues.

Additional dissipative mechanisms that can be superposed onto the HTB in the linear anelastic regime include elastically accommodated grain boundary sliding (Zener, 1941; Xu et al., 2004; Sundberg & Cooper, 2010; Jackson et al., 2006), melt squirt (O'Connell & Budiansky, 1977; Hammond & Humphreys, 2000), and dislocation damping (at constant dislocation density) (Minster & Anderson, 1980; Farla et al., 2012; Sasaki et al., 2019).

Determining the effect of melt on attenuation is difficult though a few experiments have been performed on olivine (Gribb & Cooper, 2000; Xu et al., 2004; Jackson et al.,

2004; Faul et al., 2004) and in borneol-based analogue materials (McCarthy et al., 2011; Yamauchi & Takei, 2016; Takei, 2017). The effect of melt was demonstrated to be large, though understanding which of the mechanisms above (in particular, the HTB itself, elastically accommodated grain boundary sliding, or melt squirt) remains an open question. We note the results of Yamauchi and Takei (2016) who demonstrated that substantial weakening occurred due to premelting effects as temperatures approach near-solidus values.

We consider three anelastic constitutive laws: (1) the Extended Burgers Model (EXB) of Jackson and Faul (2010); (2) The Maxwell Frequency (MXF) Scaling of McCarthy et al. (2011); and (3) the Pre-melting (PM) model of Yamauchi and Takei (2016). The latter will be the main model we present. We provide an overview of these models here but refer the reader to Havlin et al. (2021) for a more thorough summary.

The Extended Burgers Model (EXB) (labeled the "eBurgers_PSP" in the VBRc) incorporates the linear superposition of relaxation mechanisms (Fig. 2) and the frequency domain creep function, $J^*(\omega)$, is

$$\begin{aligned} J^*(\omega;\mathcal{S}) &= J_\infty(T,P)\left[1+\Delta_B\int_{\tau_L(\mathcal{S}}^{\tau_H(\mathcal{S}}\frac{D_B(\tau;\mathcal{S})}{1+\omega^2\tau^2}\mathrm{d}\tau+\Delta_P\int_{\tau_L(\mathcal{S}}^{\tau_H\mathcal{S}}\frac{D_P(\tau;\mathcal{S})}{1+\omega^2\tau^2}\mathrm{d}\tau\right] \\ &\quad +iJ_\infty(T,P)\left[\omega\Delta_B\int_{\tau_L(\mathcal{S})}^{\tau_H(\mathcal{S})}\frac{D_B(\tau;\mathcal{S})}{1+\omega^2\tau^2}\mathrm{d}\tau+\omega\Delta_P\int_{\tau_L(\mathcal{S}}^{\tau_H(\mathcal{S}}\frac{D_P(\tau;\mathcal{S})}{1+\omega^2\tau^2}\mathrm{d}\tau\right. \\ &\quad \left.+\frac{1}{\omega\tau_{\mathrm{M}}(\mathcal{S})}\right] \end{aligned} \tag{5}$$

where $i=\sqrt{-1}$ and τ_{M} is the inverse of the Maxwell frequency. The relaxation spectrum is characterized by two processes. The HTB is described by a continuous distribution of Debye peaks (or Kelvin-Voigt elements), D_B, associated with strength Δ_B, and elastically accommodated grain boundary sliding is characterized by a broad Gaussian peak, D_P and Δ_P, occurring at a distinct frequency (above the HTB). We have made clear which variables depend on $\mathcal{S}$ and note that the timescales $\tau_{L,H,\mathrm{M}}$ also depend on the thermodynamic conditions and activation energies and volumes of olivine. The VBRc provides values for the fitting parameters (the parameters independent of S and τ) from Jackson and Faul (2010).

The Maxwell Frequency Scaling (MXF) (labeled "xfit_mxw" in the VBRc) uses a polynomial fit to experimental data to find the relaxation function directly (McCarthy et al., 2011) (instead of a phenomenological model). For this model,

$$\begin{aligned} J^*(\omega;\mathcal{S}) &= J_\infty(T,P)\left[1+\int_0^\infty\frac{X(\tau;\mathcal{S})}{\tau}\frac{1}{1+(\omega\tau)^2}\mathrm{d}\tau\right] \\ &\quad +iJ_\infty(T,P)\left[1+\int_0^\infty\frac{X(\tau;\mathcal{S})}{\tau}\frac{\omega\tau}{1+(\omega\tau)^2}\mathrm{d}\tau+\frac{1}{\omega\eta(\mathcal{S})}\right]. \end{aligned}$$

Instead of a Debye peak or Gaussian for the relaxation spectrum, a piecewise function that depends on a normalized period, τ', (where $\tau'=\tau f_{\mathrm{M}}(\mathcal{S})$), is adopted. This function is a power law where $X(\tau;\mathcal{S})=\beta_i(\tau')_i^\alpha$ and $i=1,2$ dependent upon whether $\tau'\geq 10^{-11}$. We note that η_0 is that associated with steady state diffusion creep. We use the values of parameters and $X(\tau;\mathcal{S})$ provided in McCarthy et al. (2011).

The Pre-melt Model (PM) (labeled "xfit_premelt" in the VBRc) is related to the Maxwell frequency scaling but represents an extension with higher precision data, includes higher frequency data and includes the effect of premelting (as temperatures approach the solidus) (Yamauchi & Takei, 2016). As such, $J^*(\omega)$ follows the form of eq. 6 where the relaxation is instead described by the superposition of two parts: the background dissipation with the same functional form as the MXF of $X_B(\tau;\mathcal{S})=A(\mathcal{S}\tau^\alpha$ and a high frequency Gaussian peak (like in EXB, though not necessarily representing

elastically accommodated grain boundary sliding), $X_P(\tau;\mathcal{S})$, such that $X(\tau;\mathcal{S}) = X_B(\tau;\mathcal{S}) + X_P(\tau;\mathcal{S})$. These functions are more specifically functions of a Maxwell-normalized timescale, like the MXF. In both X_B and X_P a substantial increase in Q^{-1} and reduction in η_0 are incorporated as T approaches the solidus temperatures.

2.4.4 Non-linear Maxwell

We consider non-linear effects on the steady state viscosity, whereby "non-linear" refers to a power-law relationship between strain rate and stress ($n \neq 0$ in eq. 4), resulting in the apparent viscosity becoming stress dependent. Such a regime is relevant when stresses become large enough to drive production and motion of dislocations. In eq. 4 these contributions include dislocation creep and dislocation-accommodated grain boundary sliding. We use the flow laws from Hirth and Kohlstedt (2003) to consider how the stress dependency will affect our inferences of the microphysical processes activated by GIA in Section 4.2.1. In regard to Fig. 2, this effect will essentially add another steady state dashpot, η_{disl}, in mechanical series with η_0, where the steady state deformation will be dominated by the dashpot of lower viscosity.

Within the GIA literature, several authors have explored these effects (e.g. Wu, 1992; van der Wal et al., 2010, 2013; O'Donnell et al., 2017; Huang et al., 2019) using various flow laws. Some have even used GIA observables to callibrate flow law parameters (e.g.). In these studies, composite rheology (i.e., the combination of steady state diffusion and dislocation creep laws) result in a steady state viscosity often termed the *effective* viscosity. Our usage of *apparent* viscosity continues on from language in Lau and Holtzman (2019) but also intends to include both the effect of stress on viscosity as previous authors have *and* incorporate the timescale of forcing.

A non-linear *transient* regime may also be reached in which a forcing process produces dislocations, modifying the dislocation density during the process and affecting the transient response (e.g., Farla et al., 2012; Cooper et al., 2016; Thieme et al., 2018; Hansen et al., 2019). At increasing levels of stress, dislocation density increases, causing rock to weaken. If the forcing level (applied stress) is constant or changing slowly enough (quasi-static), dislocation density can be considered constant over a time step and the dislocation creep rate steady state, as characterized by numerous laboratory studies considered here (e.g., Hirth & Kohlstedt, 2003; Hansen et al., 2011). While full self-consistency regarding the role of dislocation creep would incorporate both the transient and the steady state roles of dislocations, such a constitutive model across the range of conditions of interest here does not yet exist, though much research is underway (e.g., Hansen et al., 2019).

2.5 Departure from Previous Approaches

While in the Introduction and above we have discussed contributions within the GIA community understanding the measureable consequences of both transient and non-linear rheologies, our methodology here is to (1) simultaneously consider both in a self-consistent manner; and (2) demonstrate a means of interpreting already existing viscoelastic inferences to learn about how such constraints can continuously map out the frequency dependence of uppermost mantle rheology.

For (1) it is important to emphasize that determining the thermodynamic state of Earth subsurface requires information taken at the high frequencies of the seismic band. Even within this band, slight variations produce meaningful differences in the inference of the thermodynamic state. Eventually, these inferred thermodynamic conditions will be used to predict behavior at convective timescales ($\sim$16 orders of magnitude lower). By incorporating a single, full spectrum, constitutive law to incorporate variations within high frequency seismic constraints and predict low frequency behavior, the VBRc main-

tains a level of self-consistency that is oftentimes neglected when conversions between seismic tomography models to viscoelastic structure are made within GIA calculations (e.g., Latychev et al., 2005; Goldberg et al., 2016).

For (2), while non-Maxwell rheologies have indeed been implemented for the application of GIA (e.g., Wu, 1992; van der Wal et al., 2010, 2013; Caron et al., 2017; Huang et al., 2019), here we aim to develop a means where apparent viscosity can be connected to the underlying constitutive law in continuous fashion through considering the frequency dependence of apparent viscosities.

3 Methodology

For each location we consider (ASE and AP) we have two tasks. First, we wish to predict the 1-D apparent viscosity structure, $\tilde{\eta}_{\mathrm{UUM}}(z)$, of the uppermost upper mantle (for depth, z, down to 400 km) and the apparent lithospheric thickness, $\tilde{z}_{\mathrm{LAB}}$, both as a function of frequency, ω or f. This involves determining the thermodynamic state of each location and then using the constitutive laws to determine the full spectrum mechanical properties (Section 3.1). For both the fitting and prediction of mechanical properties, a *single* full spectrum constitutive law is used for self-consistency, with comparison among the different laws. The second task is to determine the appropriate frequency band for each data point in Fig. 1 (Section 3.2). Together, this will enable comparison of the laboratory-based models to geophysical observation.

3.1 Task 1: Determination of Apparent Viscosity and Apparent Lithospheric Thickness as a Function of Frequency for each Location

We first use information obtained at seismic timescales (Section 3.1.1) to constrain $\mathcal{S}$, applying Bayesian inversion. We assume a prior distribution for the different parameters that constitute $\mathcal{S}$ and determine the posterior likelihood distribution of these parameters given the seismic observations. The VBRc – with a chosen constitutive law – serves to predict the mechanical properties (including v_{s} *at the frequency of the given seismic observation*) based on a suite of varying $\mathcal{S}$. The temperature, which is part of the state variables $\mathcal{S}$, is further constrained to follow a physically consistent plate cooling model. The maximum likelihood state variable $\mathcal{S}$ is then used to calculate the full spectrum $\tilde{\eta}_{\mathrm{UMM}}(\omega; z)$ and $\tilde{z}_{\mathrm{LAB}}(\omega)$ for each location using the *same* constitutive law that was used to constrain $\mathcal{S}$. This point is important for a self consistent prediction of both $\mathcal{S}$ and the attached full spectrum mechanical properties. Each step is detailed in Sections 3.1.1-3.1.3 and summarized in Fig. 4. While we focus on the maximum likelihood posterior model only, we discuss trade-offs between parameters in Section 4.1.2. A more detailed exploration of the solution space is an area of future study.

3.1.1 Observational constraints: Seismic Tomography and Seismic Lithospheric Thickness

For each region, we require two pieces of information: the uppermost upper mantle seismic wave speed and a lithospheric thickness estimate. We will use the tomography model of Lloyd et al. (2019) (referenced at 1 Hz) and the lithospheric thickness model of An et al. (2015) (defined at the convective timescale) (Fig. 1C,D).

At each location we extract a single v_{s} value by horizontally averaging over a radius of 50 km surrounding the locations shown by stars in Fig. 1(C,D) and vertically averaging between 200-250 km depth (gray shaded region in Fig. 6(A,B), subpanel ii). We tested several lateral (50 to 200 km) and depth (150-200, 200-250, 250-300 km) averaging length-scales and our main conclusions remained similar, though we discuss this further in Section 4.2. In the following, we focus on the results determined using a horizontal averaging radius of 50 km and depth window of 200-250 km. The extracted values

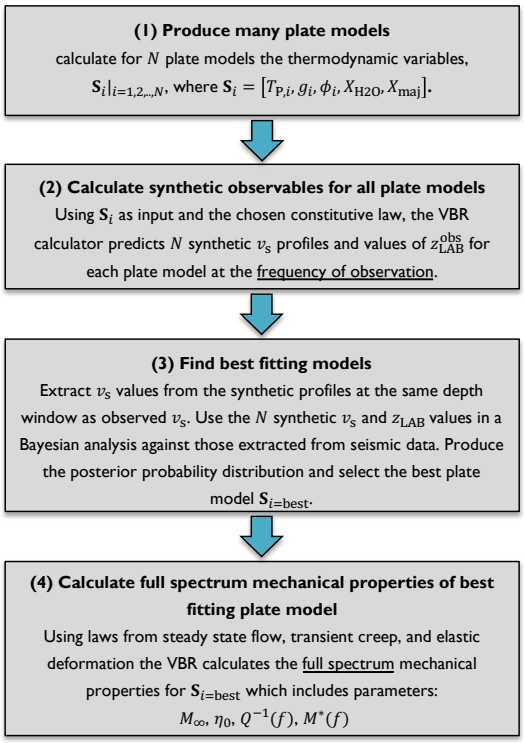

Figure 4. Methodology for Determining Viscoelastic Structure. Schematic flowchart depicting the main steps in producing full spectrum viscoelastic structure, implemented by the VBRc (Task 1, Section 3.1).

are denoted v_s^{obs} associated with ω_{obs}. We extract z_{LAB}^{obs} (at $\omega = \omega_{obs}$) from the lithospheric thickness models with the same horizontal averaging. For the uncertainty in these constraints, σ_{obs}, we have assumed ± 0.05 km/s for the wave speed measurements and ± 5 km for the LAB depth.

3.1.2 Bayesian Inference of Thermodynamic State

To determine the subsurface structure at each location down to 400 km depth, we consider depth dependent variations in thermodynamic and mechanical parameters only (localized radial stratification) and characterize this structure as a 1-D plate model. To produce a single plate model we solve the transient 1-D heat equation with variable thermal conductivity (as in Xu et al., 2004) and heat capacity (as in Berman & Aranovich, 1996) across a conductive plate to steady state using the finite difference forward model provided in the VBRc library. The solution depends on two input parameters: the potential temperature, T_P, and the thickness of the conductive lid, z_{LID}. Beneath the plate, the mantle temperature profile follows the adiabat.

We acknowledge that this is a simplification of the subsurface structure, but the smoothness of the v_s profiles (Fig. 6, subpanels ii-iii) suggests that such an approximation is reasonable and the advantage is that we can fully characterize the thermal structure with the two input parameters T_P and z_{LID}. Our aim is not to produce a detailed subsurface model, but to identify broad characteristics that might differ between our two locations. Many plate models are produced, which encompass $T_P = [1000, 1050, ..., 1800]$ °C and $z_{LID} = [50, 60, ...250]$ km. These alone characterize the temperature profile (i.e., T and P dependence) of the subsurface. In order to translate these into mechanical properties using the VBRc constitutive laws, we additionally provide uniform priors for grain size and melt fraction over the ranges $g = [0.001, 0.004, ..., 0.03]$ m and $\phi = [0.0, 0.005, .., 0.03]$, respectively. The result is a large suite of plate models which are converted to mechanical properties, like v_s and $\tilde{\eta}_{UMM}$ across the relevant frequency bands.

The Bayesian inference follows in two stages. The first is to find $\mathcal{S}$ for the depth range (gray shaded bar, Fig. 6A,B) across which we extract v_s^{obs}. This constraint will be compared to forward predictions of the plate temperature profiles at the same depth, narrowing down the range of plausible plate profiles. The second is to use z_{LAB}^{obs} to constrain z_{lid} from the subset of remaining plate models.

Given v_s^{obs}, associated with the depth range, we determine posterior distributions of the state variables ϕ, T, and g (melt fraction, temperature, and grain size). The statement of our inference is

$$P(\mathcal{S}|v_s^{obs}) = \frac{P(v_s^{obs}|\mathcal{S})P(\mathcal{S})}{P(v_s^{obs})} \tag{6}$$

where $P(\mathcal{S}|v_s^{obs})$ is the posterior probability that represents how well constrained the state variables of interest are given v_s^{obs}, $P(v_s^{obs}|\mathcal{S})$ is the likelihood that describes how likely v_s^{obs} is given $\mathcal{S}$, $P(v_s^{obs})$ is the probability of observing the measurement itself (used here as a normalizing factor), and $P(\mathcal{S})$ is the prior distribution of the state variables. $P(v_s^{obs}|\mathcal{S})$ is determined from a χ^2-misfit with which we construct a Gaussian likelihood matrix where

$$P(v_s^{obs}|\mathcal{S}) = \frac{1}{\sqrt{2\pi\sigma_{obs}^2}} \exp\left(\frac{\chi^2}{2}\right), \tag{7}$$

and

$$\chi^2 = \frac{[v_s^{obs} - v_s(\omega_{obs}; \mathcal{S})]^2}{\sigma_{obs}^2}. \tag{8}$$

Here, σ_{obs} is the uncertainty in the observation. To construct $P(v_s^{obs}|\mathcal{S})$ we use the VBRc to calculate $v_s(\omega_{obs}; \mathcal{S})$ from our plate model suite. For our prior distribution of the state variables we assume a uniform probability across all state variables (where the search range is noted above) and treated as independent of each other for simplicity.

To determine the lithospheric thickness we use the same Bayesian inference framework but the observation is now $z_{\mathrm{LAB}}^{\mathrm{obs}}$. With many definitions for the LAB, $z_{\mathrm{LAB}}^{\mathrm{obs}}$ may not be equivalent to z_{LID}. Such definitions include the depth at which the largest negative value of $\partial v/\partial z$ occurs (Hopper & Fischer, 2018) or the maximum depth for which v_{s} anomalies are consistently greater than 2% (Conrad & Lithgow-Bertelloni, 2006). See Lau et al. (2020) for further discussion. However, the lithospheric thickness model of An et al. (2015) define $z_{\mathrm{LAB}}^{\mathrm{obs}}$ as the intersection of the base of the conductive lid, and so in this case, this definition is precisely z_{LID}. The misfit in this case is calculated as:

$$\chi^2 = \frac{[z_{\mathrm{LAB}}^{\mathrm{obs}} - z_{\mathrm{LID}}(\omega_{\mathrm{obs}}; \mathcal{S})]^2}{\sigma_{\mathrm{obs}}^2}. \tag{9}$$

For our analysis below, we will select the profile of $\mathcal{S}(z)$ that maximizes $P(z_{\mathrm{LAB}}^{\mathrm{obs}}|\mathcal{S})$.

3.1.3 Determination of Apparent Viscosity and Apparent Lithospheric Thickness

With $\mathcal{S}(z)$ determined, the VBRc is used, with $\mathcal{S}(z)$, to output the full-spectrum profiles of $M^*(\omega)$, $Q^*(\omega)$, and $\eta^*(\omega)$ at each location. Using the latter, we introduce two simple parameters: the apparent viscosity $\tilde{\eta}(\omega)$, which is the absolute value of the complex viscosity and the apparent lithospheric thickness, $\tilde{z}_{\mathrm{LAB}}$. For $\tilde{z}_{\mathrm{LAB}}$, within any column of mantle rock, we may determine the Maxwell time as a function of depth ($\tau_{\mathrm{M}}(z)$), since this is the ratio of two depth-dependent material properties, $\eta_0(z)$ to $M_\infty(z)$. If we are interested in $\tilde{z}_{\mathrm{LAB}}$ at a given frequency, we find the depth at which τ_{M} is equivalent to this frequency. This essentially marks the transition from elastic to viscous behavior for this frequency. This definition breaks down if the frequency is higher than any Maxwell frequency in the mantle, where we propose that $\tilde{z}_{\mathrm{LAB}}$ becomes essentially frequency independent. At these high frequencies the notion of a plate itself becomes unclear. We note that this is just one definition of many that exists for the LAB, though this definition highlights the frequency dependence of $\tilde{z}_{\mathrm{LAB}}$.

As is common in GIA studies that consider non-linear rheologies (e.g., van der Wal et al., 2010), we reinterpret the reported values of "η" and "z_{LAB}" presented in Fig. 1 as *apparent* quantities, (where apparent lithospheric thicknesses are explored in greater detail in Lau et al. (2020) and we only briefly describe the method by which we determine $\tilde{z}_{\mathrm{LAB}}$ below).

3.2 Task 2: Determining Frequency Content of Observed Inferences of Uppermost Upper Mantle Viscosities and Lithospheric Thicknesses

Observationally derived estimates of lithospheric thickness and viscosity are generally obtained by combining knowledge of past load changes (ice sheets or lakes) with observations of deformation (GPS or reconstructions of paleo-water level) assuming a viscoelastic model. The estimates we have used for comparison against our VBR-driven profiles are all parameters reported from studies which applied geodetic constraints, and thus are subject to a range of simplifying assumptions. The estimates of both z_{LAB} and η_{UMM} have been compiled from the following investigations for each region (listed in order of decreasing timescale): For Amundsen Sea Embayment, we include the results from Whitehouse et al. (2012), who used relative sea level data to study the effects of long term GIA across the entire Antarctica region (and select their reported values associated with the ASE) and from Barletta et al. (2018), who used GPS derived measures of decadal-scale rebound at the Amundsen Sea Embayment. For the Antarctic Peninsula, decadal (Nield et al., 2014; Samrat et al., 2020) and centennial (Ivins et al., 2011; Wolstencroft et al., 2015) responses to ice mass change, once more measured by GPS, were used to derive viscosity estimates.

We will also investigate z_{LAB} estimates derived from gravity-based data of Chen et al. (2018). These provide effective elastic thickness estimates of the Antarctic plate and should be interpreted as the thickness of a completely elastic lid overlying an inviscid mantle (where $\tilde{\eta}_{\mathrm{UMM}} \to 0$). Such a result would be relevant at zero frequency. For a more detailed discussion on this matter, see Lau et al. (2020).

In order to compare our predictions of $\tilde{\eta}_{\mathrm{UMM}}(\omega)$ and $\tilde{z}_{\mathrm{LAB}}(\omega)$ to the observations presented in Fig. 1, we need to determine their appropriate frequency content. In all the cases, the data points fit were uplift rates extracted from a time series of GPS data. These single uplift rates were used to determine z_{LAB} and η and capture a whole range of frequencies embedded in not only the loading history (here, approximated by τ_{dur}, the duration over which the loading/unloading event in question occurred) but also the delay in measuring the response (here, approximated by τ_{del}, the time delay between the end of the event and when the observation of solid Earth deformation was made). For example, in Barletta et al. (2018), one of their analyses involved investigating the change in ice loss between 2002-2014 and GPS measurements were made throughout this time. In this case, $\tau_{\mathrm{dur}} = 12$ years and $\tau_{\mathrm{del}} = 0$ years. These designations of τ_{del} and τ_{dur} – tabulated and summarized for each observation in Table A1 – are approximate and our aim is to cover a wide enough frequency band to provide the most conservative estimate possible.

We will use these two important timescales to determine an appropriate frequency band, $[f_{\mathrm{low}}, f_{\mathrm{upp}}]$. For f_{upp} we know that, given the timescale of any process, the highest possible frequency must be bound by τ_{dur}^{-1}. The Fourier transform of a linear trend is dominated by these low frequencies and longer values of τ_{del} will result in any relatively high frequency response to diminish. But just how low is this bound? We will determine this lower bound by applying an empirical relationship based on replicating the loading history and measurements of deformation.

For this empirical relationship, we replicate the loading histories of our observations, $\sigma(t)$, apply this stress load to a given material of compliance J and calculate the deformation, i.e., the strain, $\varepsilon(t)$. The compliance will be that associated with our upper mantle structures beneath ASE and AP (trends shown in Figs 6v,vi). Our generic stress history is depicted in Fig. 5(A).

There are two ways in which we may determine $\varepsilon(t)$. We could perform this calculation in the Fourier domain and multiply the stress history with $J^*(\omega)$ and take the inverse Fourier transform to produce the time domain response. This seems ideal since from experimental results, as output by the VBRc, we readily know $J^*(\omega)$. However, several factors complicate this approach: the frequency range in which we sample both $\sigma^*(\omega)$ and $J^*(\omega)$ are naturally entirely different (where the former is linear, whereas the latter is logarithmic) and inverting the Fourier transform with either of these options presents some limitations (see, e.g., Haines & Jones, 1988).

Instead, we choose to convolve the stress history with $J(t)$. That is,

$$\varepsilon(t) = \int_{-\infty}^{t} J(t - t')\mathrm{d}\sigma(t'). \tag{10}$$

Given that only $J^*(\omega)$ is determined by the VBRc and not $J(t)$, we obtain $J(t)$ by fitting $J^*(\omega)$ to that of an Andrade viscoelastic model, $J^*_{\mathrm{An}}(\omega)$ (Fig. 2). We choose the Andrade model since it can capture the full spectrum of viscoelastic (elastic, transient, viscous) behavior with few model parameters (Cooper, 2002) where expressions for $J^*_{\mathrm{An}}(\omega)$ and $J_{\mathrm{An}}(t)$ are given by

$$J_{\mathrm{An}}(t) = \frac{1 + t/\tau_{\mathrm{M}}}{M_\infty} + \beta t^n \tag{11}$$

and

$$J^*_{\mathrm{An}}(\omega) = J_\infty + \beta\Gamma(1+n)\omega^{-n}\cos\left(\frac{n\pi}{2}\right) - i\beta\Gamma(1+n)\omega^{-n}\sin\left(\frac{n\pi}{2}\right) + \frac{1}{\eta_0\omega} \tag{12}$$

(Faul & Jackson, 2015). Here, Γ is the standard gamma function of order n, where typical values of n are 1/3 (Cooper, 2002). For each of our regions, τ_{M}, J_∞, M_∞, η_0, and $J^*(\omega)$ are provided by the VBRc. β determines the strength of the anelastic contribution and thus once knowledge of β is acquired, calculating $J_{\mathrm{An}}(t)$ is trivial.

We solve for the best fitting β via a grid search and the resulting $\tilde{\eta}(\omega)$ values for each region are shown in Fig. 5(B). The solid lines are reproduced from Fig. 6 (subpanels v). With the simple time domain expression for $J_{\mathrm{An}}(t)$ we can readily perform the convolution in eq. 10.

We apply the linearly increasing load for a period of τ_{dur} depicted in Fig. 5(A) and perform many tests across the range $(10^{-2} \leq \tau_{\mathrm{dur}} \leq 10^{6})$ years, effectively varying the stress rate, and convolving this with the best-fitting $J_{\mathrm{An}}(t)$ expressions (Fig. 5B). In order to emulate measurements made by the unloading/loading scenarios in our dataset, we determine the resulting strain rate, $\dot{\varepsilon}$, from Eq. 10. We calculate $\dot{\varepsilon}$ values at various values of τ_{del} across the range $(10^{-4}\tau_{\mathrm{dur}} \leq \tau_{\mathrm{del}} \leq 10^{4}\tau_{\mathrm{dur}})$ years, a range that covers all scenarios. Using the strain rate, we estimate the viscosity assuming a *Maxwell viscoelastic model* for which η_{est} can be calculated as (for the simple 1-D case)

$$\eta_{\mathrm{est}} = \sigma \left(\dot{\varepsilon} - \frac{\dot{\sigma}}{M_\infty} \right)^{-1}. \tag{13}$$

As argued previously, these viscosity estimates are capturing the apparent viscosity of the underlying Andrade model, i.e., $\tilde{\eta}_{\mathrm{An}}$, at its respective frequency. We can therefore estimate f_{low} as the frequency for which $\tilde{\eta}_{\mathrm{An}}$ is equivalent to η_{est}. For each observation, we show the frequency band dictated by τ_{dur} and τ_{del} in Figs 5(C,D).

4 Results and Discussion

4.1 Resulting Subsurface Structure

In our main result (Fig. 6) we show the predictions of the anelastic model of Yamauchi and Takei (2016) (the "Pre-melt Maxwell-scaled" model, PM) and we discuss the subsurface structure in Section 4.1.1. In Section 4.1.2 we show the differences in both the thermodynamic constraints and the frequency dependent mechanical parameters that arise if we repeat the VBRc calculations with two other anelastic models, the Extended Burgers (EXB) model of Jackson and Faul (2010) and the Maxwell Frequency Scaling (MXF) model of McCarthy et al. (2011) (a predecessor of the PM model).

4.1.1 Results from Pre-melt (PM) Model

The resulting steady state viscosity (colored lines) and temperature (black lines) profiles are shown in Fig. 6, subpanels iv. The resulting T_P for ASE and AP are 1800 °C and 1700 °C, respectively. These are above the temperatures for average mantle, but somewhat in line with other estimates of sublithospheric mantle temperature. For example, the temperature model of An et al. (2015) beneath ASE at the depth range we constrain is in the similar range. However, they too converted seismic wave-speeds to temperature so any comparison most likely reflects the choice of conversion. An et al. (2015) used the empirical scalings determined by Goes et al. (2000), which estimated temperature-composition-seismic wave-speed relations using seismic wave-speed data across Europe and laboratory results.

The steady-state viscosity profiles (Fig. 6, subpanels iv) of each region show the structure most relevant to mantle convection timescales. The steady state viscosity structure is approximately 10^{20} Pa s and 3×10^{21} Pa s averaged across our domain. These results are in accord with results from O'Donnell et al. (2017) who once more used seismic wave-speeds to estimate the thermodynamic structure, but incorporated laboratory

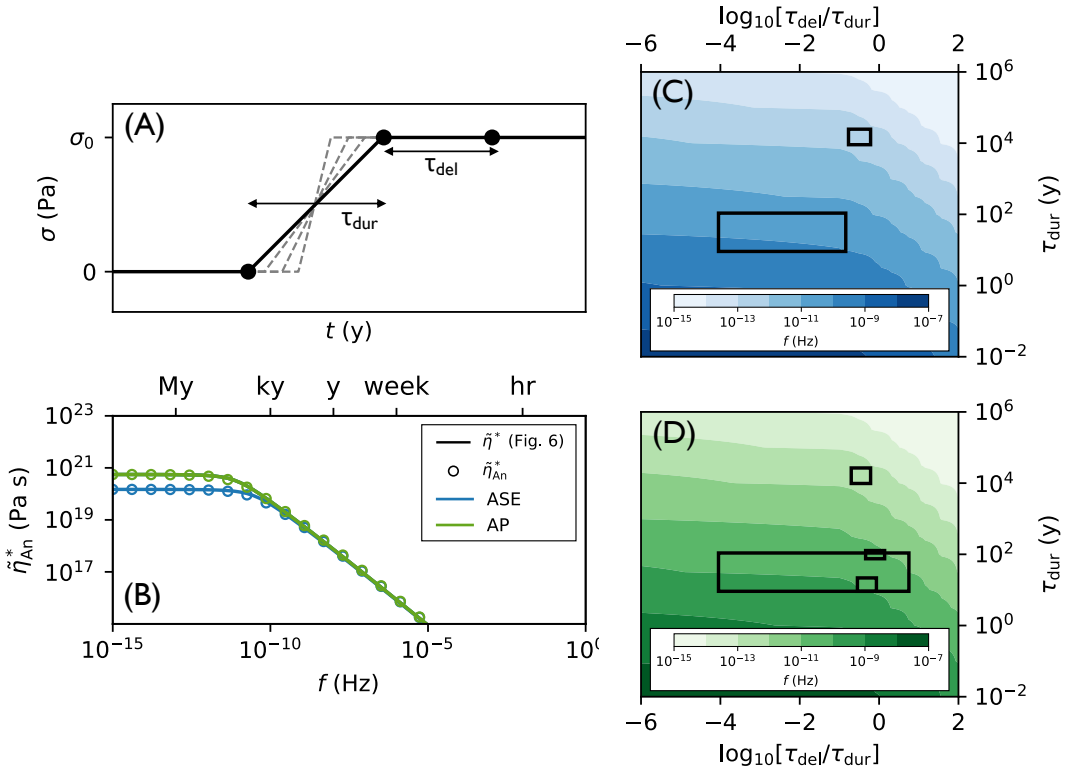

Figure 5. Converting time domain observations to the frequency domain. (A) Schematic depiction of applied stress history, $\sigma(t)$, labelling the two relevant timescales, $\tau_{\rm dur}$ and $\tau_{\rm del}$. (B) The apparent viscosities for each region of the 1-D Andrade model that $\sigma(t)$ is applied to. The solid lines are reproduced from Fig. 6(subpanels v) and circles are the result of finding the best fitting Andrade parameters for each region. (C,D) Contours mark the frequency for which the estimated $\tilde{\eta}_{\rm est}$ (assuming a Maxwell) is equivalent to $\tilde{\eta}_{\rm An}$ (i.e., where $\tilde{\eta}_{\rm est} = \tilde{\eta}_{\rm An}(f_{\rm An})$ for ASE (C) and AP (D)). The boxes are the associated $\tau_{\rm dur}$ and $\tau_{\rm del}$ ranges for each observation we include (see Fig. 1).

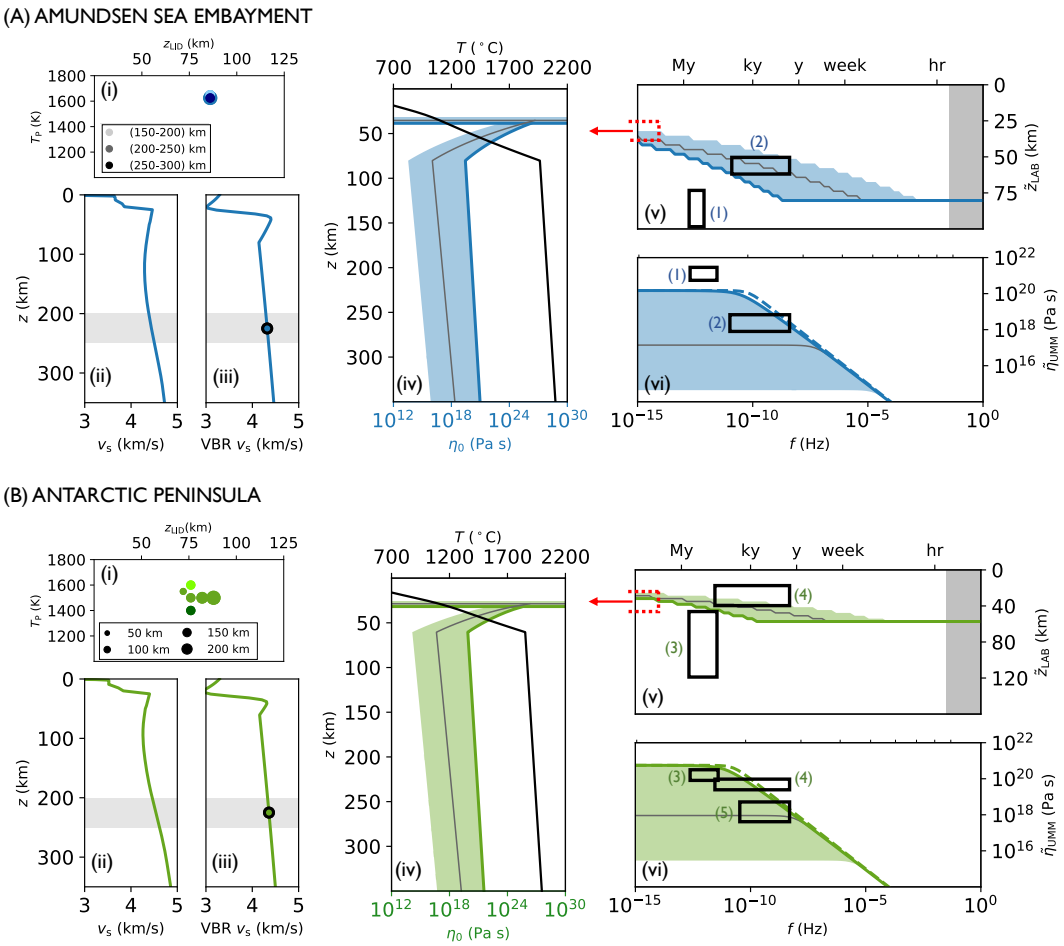

Figure 6. Resulting Thermodynamic and Mechanical Properties for Case Regions. For each region (A) and (B), subpanel (i) shows best-fit potential temperature-plate thickness pairs for differing horizontal and vertical averaging length-scales. The legend in A(i) corresponds to depth and in B(i) to horizontal length-scales and both legends are associated with the two subpanels (i). Subpanel (ii) shows the shear wave-speed, v_s, profiles at select regions in Fig. 1(C,D) (averaged over a lateral radius of 50 km) of the tomography model of Lloyd et al. (2019). The gray shaded region marks the depth window across which we used v_s to constrain uppermost upper mantle temperature, where circles mark the resulting v_s from the fitting procedure. (We tested other depth windows shown in panel (i).) Subpanels (iii-vi) are generated by the VBR fitting procedure (see Fig. 4, where (iii) shows the v_s profile of best fitting plate model, while (iv) shows the associated temperature profile (solid black line). The following corresponding mechanical properties are: (iv) the steady state viscosity η_0 (solid colored line) where horizontal lines mark the base of the lithosphere; (v) the apparent lithosphere-asthenosphere boundary, $\tilde{z}_{\mathrm{LAB}}$, and (vi) the apparent uppermost upper mantle viscosity, $\tilde{\eta}_{\mathrm{UMM}}$, as a function of frequency, f, averaged across the depth of the domain (base of lithosphere to 400 km). In addition, the effect of steady state dislocation creep on these parameters across a stress range ($0 \leq \sigma \leq 10$ MPa) in denoted by the shaded regions (iii-vi). The solid colored and gray lines coincide with $\sigma = 0$ MPa and 1 MPa, respectively. The black boxes are the observationally derived estimates from Fig. 1. References are labeled: (1) Whitehouse et al. (2012); (2) Barletta et al. (2018); (3) Wolstencroft et al. (2015); (4) Ivins et al. (2011); (5) Samrat et al. (2020); The vertical gray shaded region spans the seismic band within which the thermodynamic conditions were constrained. The dashed red open box in subpanel (v) denotes an estimate of effective elastic thickness of Chen et al. (2018). In (vi) the dashed lines are the predictions of $\tilde{\eta}_{\mathrm{UMM}}$ with equivalent Maxwell model (η_0 and M_∞) without transient elements.

scalings of Hirth and Kohlstedt (2003), Hansen et al. (2011), and Ohuchi et al. (2015) (for dislocation processes). Given the similarity of chosen flow laws, this is to be expected.

Turning now to frequency dependence of $\tilde{\eta}_{\mathrm{UMM}}$, we see that this parameter can vary significantly for different frequencies (Fig. 6 (v) and (vi) colored solid lines). In both locations, the predicted $\tilde{\eta}_{\mathrm{UUM}}$ decreases as a function of increasing frequency, which would result in higher frequency processes deforming a less viscous mantle.

The horizontal-colored line in Fig. 6, subpanels iv, shows the depth at which $\tilde{z}_{\mathrm{LAB}}$ occurs at the zero-frequency limit. This can be thought of as the true thickness of the plate – which, by many definitions within the literature, is the base of the top thermal boundary layer of mantle convection (Fischer et al., 2010). However, as Lau et al. (2020) argue, many studies infer *apparent plate thickness* at the frequency of the unlodaing process (colored bold lines, subpanels v). For example, changes in seismic velocity gradients, seismic anisotropy measurements, receiver functions and attenuation data (e.g. Hopper & Fischer, 2018; Mancinelli et al., 2017) have been used to infer $\tilde{z}_{\mathrm{LAB}}$ at frequencies of $\sim (0.01-0.1)$ Hz. This inference of $\tilde{z}_{\mathrm{LAB}}$ lies towards the far right of subpanel v (gray bar). The physical relationship between the seismic LAB and the convective LAB is discussed in more detail in Lau et al. (2020). As can be seen, moving towards lower frequency, $\tilde{z}_{\mathrm{LAB}}$ relaxes to significantly shallower depths as the asthenosphere beneath becomes increasingly viscous, impinging on the rigid plate above. At high frequency, we find that $\tilde{z}_{\mathrm{LAB}}$ is at a maximum as hotter conditions (i.e., deeper depths) must be reached for the elastic-to-viscous transition to occur. These panels demonstrate that one cannot assume that LAB values inferred on seismic timescales are appropriate for processes acting on convection or GIA timescales. An analogous discussion based on the Effective Elastic Thickness of plates at different timescales can be found in Watts et al. (2013).

While lateral variations in thermodynamics and the potential variability in the sampled subsurface of each observation can contribute to the variability in z_{LAB} and η_{UMM} within each region (including artefacts introduced as a consequence of inferring localized radially stratified (1-D) versus laterally variable (3-D) viscosity structures, see e.g., van der Wal et al., 2015; Lau et al., 2017; Crawford et al., 2018; Powell et al., 2020), our comparison between these observation-driven estimates and VBRc determined predictions of frequency dependent parameters illustrates that such processes are not only important to consider, but can possibly explain some of the variation in GIA-based estimates. We therefore suggest moving towards a framework that aims to map the continuous frequency trend of $\tilde{\eta}(\omega)$ through observations occurring at different frequencies – akin to mapping out the frequency dependence of $Q^{-1}(\omega)$ in seismic studies (Fig. 3). If a complete trend may be mapped, more concrete inferences about the underlying viscoelastic model may be made. However, unlike the seismic application, quantifying the frequency content for any given time-domain GIA process is not trivial and while we propose one approach here (Section 3.2), we argue that further work is required to better understand this relationship.

4.1.2 Sensitivity of Thermodynamic State to other Experimental Constitutive Laws

The anelastic constitutive model adopted has a strong influence on the determined thermodynamic state. For instance, the PM model results in much lower UMM temperatures than both the MXF and EXB models, but the difference is somewhat more pronounced between PM and EXB (compare subpanels (iii) in Fig. 7). As previously mentioned, this is likely due to the premelting effects included in PM which incorporates significant weakening behavior as temperatures approach the solidus. As such, to account for any dispersion effects of v_{s} at f_{obs}, this additional weakening means that temperatures need not be so elevated as in the two models without premelting mechanisms.

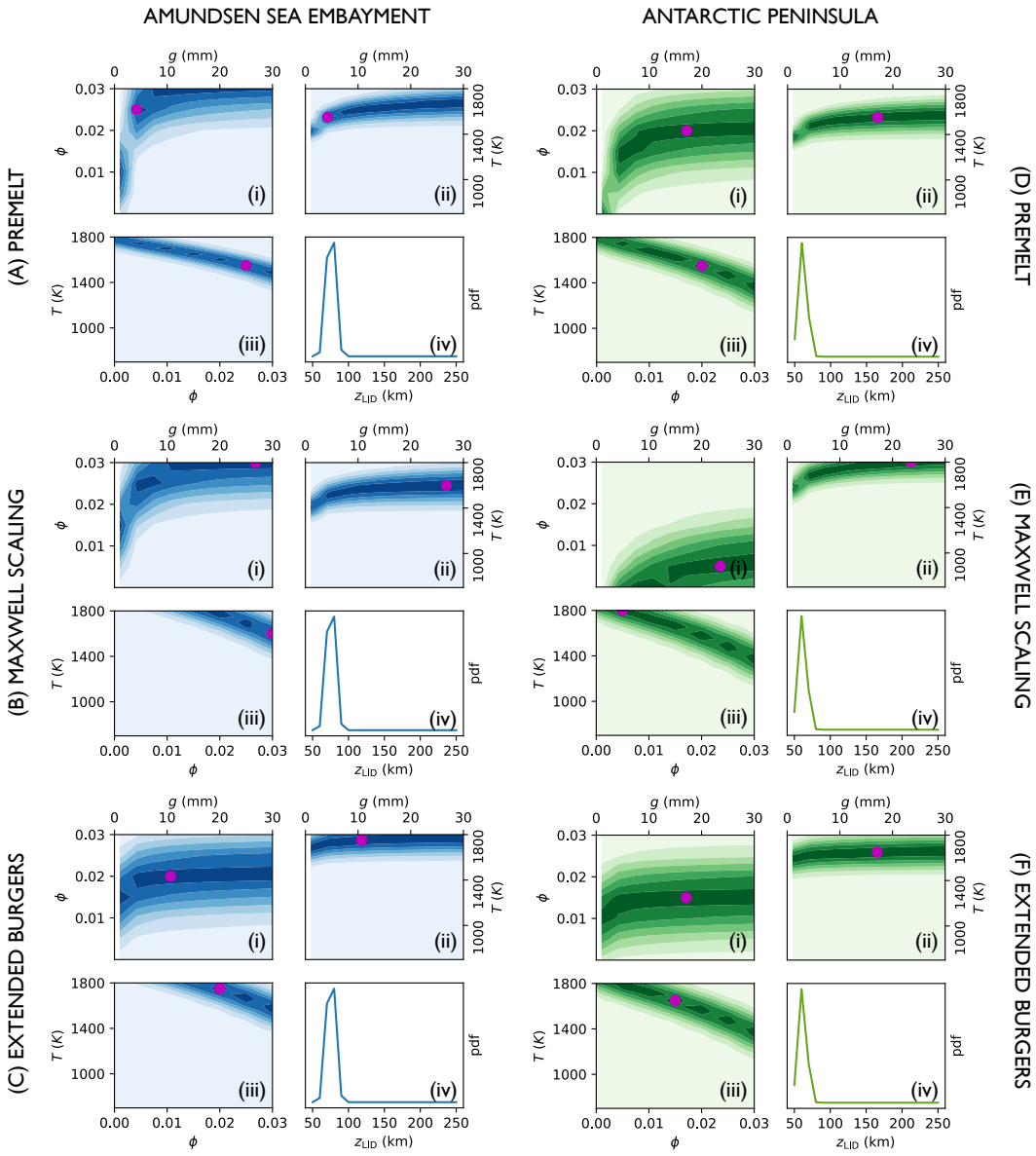

Figure 7. Joint Posterior Probability Distributions of Thermodynamic Conditions. For ASE (left panels) and AP (right panels), each row represents the anelastic model used. Subpanels (i-iii) display the joint posterior probability distributions for fitting v_s between 200-250 km depth (shaded bars in Fig. 5A.ii,B.ii) between temperature, T, grain size, g, and melt fraction, ϕ, as described in Section 3.1.2. The more intense colors denote increasing likelihood. The green dot is the maximum posterior probability. Subpanels (iv) display the posterior probability distribution of the thickness of the conductive lid, z_{lid}.

Trade-offs between grain size and the other parameters are also significantly different between PM/MXF and EXB. The former two have a grain size exponent of 3, related to the direct incorporation of the steady state diffusion creep viscosity; thus the region of high likelihood shows significantly more curvature than that of EXB, which has a grain size exponent of 1.2. See subpanels (i-ii). For PM and MXF, if grain size was a known quantity, determining T and ϕ becomes much more tightly constrained. The importance of the role of grain size (and subgrain size) in dissipation mechanism remains an open question with many implications for the estimation of melt fraction, ϕ. All models show negative covariance between T and ϕ, which is to be expected. Havlin et al. (2021) demonstrated that placing a strong prior has a significant effect on the temperature estimates, but because we are focused here on the viscosity trade-offs, not the temperature inference, we leave this level of complexity for future work.

While we have used a completely forward modeling approach adopting standard constants as published for each anelastic constitutive models, an alternative method was used by Richards et al. (2020); Austermann et al. (2021). Using independent constraints on the thermodynamic structure of the upper mantle, they adopted the PM parameterization but calibrated several constants to given seismic observations. Interesting questions arise in regard to the lab-to-earth time scaling and to the degree of spatial homogenization between a laboratory-based grain-scale observation versus the macroscropic observation made as a seismic wave passes through mantle rock. This point is further elaborated on in the next section. The union of these two approaches, however, may provide a new path forward towards further constraining rheological laws.

4.2 Predicted and Observed Frequency Dependencies: grain-scale processes and their manifestation in GIA

In Fig. 6 we have also placed the apparent viscosities and plate thicknesses obtained from observational estimates (Fig. 1) in order to compare them against our modeled predictions. Across all regions some of the observations of $\tilde{\eta}_{\mathrm{UMM}}$ (subpanels vi) fit the predicted values well (colored solid lines) and some fall within the shaded regions, which we discuss in Section 4.2.1. A slightly less clear picture is seen with $\tilde{z}_{\mathrm{LAB}}$ (subpanels v), where several observations do not align with the predictions (solid colored lines). We note that $\tilde{z}_{\mathrm{LAB}}$ observations and predictions are particularly mismatched for AP. Here, we point to the inherent variability of this region and note that a greater degree of scatter exists for T_{P} and z_{LID} when choosing different lateral and depth averaging length-scales (compare Fig. 6B.i with 6A.i). As such, the lateral structure could be significantly contributing to the differences in observed $\tilde{z}_{\mathrm{LAB}}$ values, which is not captured by our simplistic local stratified model. In particular, it is important to consider that the continental lithosphere is comprised of a narrow peninsula rather than a large continental interior and the observations we selected span the stretch of the entire Peninsula. In addition, slightly beneath the depth range we consider, there is a subducting slab that may also affect GIA (Lloyd et al., 2019).

The non-loading related observations of effective elastic lithospheric thickness (Chen et al., 2018) appear as dashed red open boxes in Fig. 6, subpanel (v). The arrow attached denotes that such thicknesses are to be interpreted as the thickness are associated with the $\omega = 0$ endmember. As can be seen, these results are largely consistent with our predictions. This suggests that the steady state predictions of z_{LAB} from the viscous portion of the constitutive laws are relatively well calibrated with the Earth scale.

4.2.1 Diffusion and Dislocation Creep

What might we infer from these results about the activation of certain deformation mechanisms at the grain-scale?

The solid lines in Fig. 6 mark rheological parameters for which the underlying mechanism is diffusion creep. In GIA, the most commonly adopted viscoelastic model used to phenomenologically describe such creep is the Maxwell model (as is the case with all the observations included here). Now we assess the degree to which transient creep may contribute to the trend in $\tilde{\eta}(\omega)$ captured by our selected observations.

The solid colored lines in subpanels vi capture the trend of Pre-melt Maxwell-scaled model of Yamauchi and Takei (2016). The dashed colored lines are identical but with no transient creep component (i.e., no HTB), representing a Maxwell model with the same η_0 and M_∞ values. The departure from $\tilde{\eta}$ between the Pre-melt and its Maxwell-only equivalent clearly occurs across a frequency band spanned by most of the processes we consider. While these discrepancies in $\tilde{\eta}$ seem slight in the figures, the differences between these two models can be significant, e.g., a factor of $\sim$ 2.3 at 10^{-10} Hz and $\sim$ 2.6 at 10^{-12} Hz for ASE and AP, respectively. These factors are emphasized in the plots of normalized $\tilde{\eta}$ in Lau et al. (2020). Our data here cannot distinguish the difference between the two trends of $\tilde{\eta}_{\mathrm{UMM}}$ but future studies may be designed to identify the degree of HTB transient creep and explore additional dissipative mechanisms in such deformation. An additional point to note is that while for the $\tilde{\eta}$ parameter, differences between the inclusion of the full anelastic model versus the Maxwell-equivalent is most prominent across the GIA frequency band, for $Q^{-1}(\omega)$, these differences are significant in the seismic band. These differences will likely affect the way our thermodynamic setting is inferred (see Section 3.1).

Transient diffusion creep rate is linear in stress and relevant at low levels of both strain and stress, where deformation probes the microstructure but does not modify it. Processes like GIA and seismic wave propagation are characterized by small strains ($\sim 10^{-5}$) and low stresses ($\sim$kPa), such that it is possible that transient diffusion creep dominates any transient response, and likely that grain sizes are not altered by those processes.

Towards estimating the potential effects of dislocation creep in the wide-band responses considered here, we incorporate steady state dislocation creep into the our results in Fig. 6 (without considering the transient role of dislocations). In subpanels (iv-vi) of Fig 6, shaded regions reflect the effect of steady state dislocation creep (Hirth & Kohlstedt, 2003) and encompass variations in η_0, $\tilde{\eta}_{\mathrm{UMM}}$, and $\tilde{z}_{\mathrm{LAB}}$ for stresses ranging ($0 \leq \sigma \leq 10$) MPa (where bold colored lines and fine gray lines coincide with 0 and 1 MPa, respectively). As shown by these regions, macroscopically, there is a reduction in the value of all parameters (Fig. 6) and the transition of $\tilde{z}_{\mathrm{LAB}}$ is shifted to higher frequency as the effective Maxwell time is now reduced. We note that, in certain parts of the plate, GIA processes reach such levels of stress (in Fig. A1 we show the deviatoric stress beneath the ice sheet over a representative GIA cycle). Since several of the observations fall within these shaded regions, it is possible that non-linear deformation is occurring to explain these estimates of $\tilde{\eta}$ and $\tilde{z}_{\mathrm{LAB}}$. These steady state effects across Antarctica have been shown to be significant (though without the consideration of transient creep) by, e.g., van der Wal et al. (2015), and for the lithosphere, by Nield et al. (2018).

4.2.2 Can Observations Distinguish Between Experimental Constitutive Laws?

Using the maximum likelihood thermodynamic parameters in Fig. 7 (pink circles), predictions of $\tilde{\eta}_{\mathrm{UMM}}(\omega)$ and $\tilde{z}_{\mathrm{LAB}}(\omega)$ using each anelastic model PM, EXB, and MXF were made. Fig. 8 shows the result (where the PM result is identical to that in Fig. 6). The frequency axis focuses on the lower frequency half of the results shown in Fig. 6. Unlike the thermodynamic parameters which show a large variation between the three anelastic constitutive laws, what is predicted at the macroscale is largely similar.

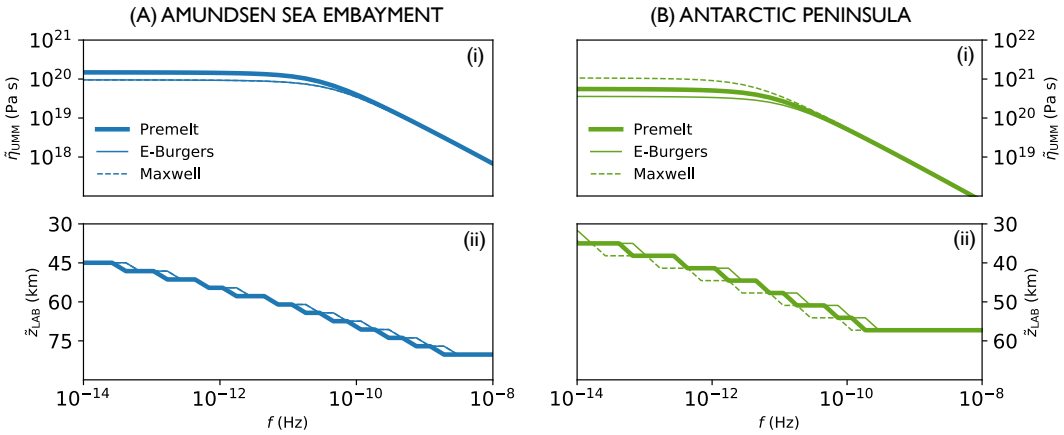

Figure 8. Comparison of Apparent Viscosity and Lithospheric Thicknesses Between different Anelastic Models. The frequency dependent predictions of $\tilde{\eta}_{\mathrm{UMM}}$ (i) and $\tilde{z}_{\mathrm{LAB}}$ (ii) for ASE (A) and AP (B) using the Pre-melt Maxwell-scaled model (Yamauchi & Takei, 2016), the Extended Burgers model (Jackson & Faul, 2010), and the Maxwell-scaled model (McCarthy et al., 2011). These were calculated using the maximum likelihood thermodynamic parameters in Fig. 7.

Indeed, within the uncertainty of the observations, it would be difficult to distinguish between the three models. Thus, determining which anelastic constitutive laws are more accurate may be difficult to constrain using macroscopic observations, since the trade-offs result in largely similar behavior across frequency. As suggested previously, between the approach of calibrating experimental parameterizations from macroscopic observations, like seismic data, it is clear that care must be taken and the conjunction of such an approach with the kind we have performed here provides a fruitful avenue of further investigation.

4.3 Implications for Ice Mass and Sea-level Change

Ice mass change, both past and present, span a wide frequency spectrum, and we show here that so too does the variation of the solid Earth's response to such perturbations. Based on our results, we suggest that by reinterpreting estimates of viscosity and plate thickness as *apparent viscosities* and *apparent plate thicknesses* and accounting for their frequency content may explain some of the variability in the values presented Fig. 1A,B. We also note that laboratory-based constitutive laws suggest that transient creep may play some role across the span of our observations (from rapid to ∼10 ky timescales).

Ultimately, ignoring deformation mechanisms acting across the wide frequency range of GIA processes may lead to mis-estimation of the sea-level response, whether those include rapid ice collapse, where studies typically invoke a purely elastic Earth (lithosphere *and* convecting mantle) (e.g., Gomez et al., 2010) or solid Earth responses modeled purely as Maxwell viscoelastic solids. For example, following our results shown in Fig. 6A, we predict that if the same amount of ice retreat in the Amundsen Sea area occurred over 1, 10, 100, and 1000 y, the uppermost upper mantle apparent viscosity would be $\sim 5\times 10^{17}$, $\sim 2\times 10^{18}$, $\sim 10^{19}$, and $\sim 7\times 10^{19}$ Pa s, respectively.

In not too dissimilar a region, Nield et al. (2016) demonstrated that, at the Siple coast, the importance of short term ice redistribution like the stagnation and reactivation of ice streams ($\sim$ 100 years) to crustal uplift, depends intimately on whether subsurface viscosity was below a certain threshold. On the Eastern side of the continent,

King and Santamaría-Gómez (2016) explored the use of a Burgers rheology to explore the postseismic viscoelastic response. These studies represent other examples of the interactions between differing timescales of forcings and Earth's mechanical response and thus all these findings may have implications for the stabilizing effect of GIA on the Antarctic ice sheet, which affects predictions of future sea level change.

A further compounding factor on all timescales is that high frequency and high magnitude melt events will result in high strain rates, which may require the consideration of non-linear rheology that involves changes in the dislocation structure driven by these large external stresses. It is unclear how such extraneous stress regimes might alter GIA during these events, but one might expect that the apparent viscosity would be significantly reduced due to stress magnitude and the relatively high frequency of such intense melting events. So far non-linear rheologies have only been considered in isolation (Wu, 1992; van der Wal et al., 2010, 2013; Huang et al., 2019), but our preliminary calculations presented here show that these effects have repercussions across a wide frequency band.

5 Conclusions

The adoption of the Maxwell viscoelastic models derived from the early semi-analytical techniques (Wu & Peltier, 1982; Mitrovica & Milne, 2003) offered an elegant means to solve a complicated viscoelastic system and fit a whole range of sea-level and geodetic observations. The realization, however, that temperature effects alone result in lateral variations in viscosity that span orders of magnitude required a distinct departure from these semi-analytic techniques and a movement towards computationally demanding finite-element methods that continues today (e.g., Wu & van der Wal, 2003; Zhong et al., 2003; Latychev et al., 2005).

With a growing richness in datasets that capture increasingly subtle signals of ice melt, we believe the next level of complexity must be met. Our results outlined here have highlighted a potential pathway towards considering both thermodynamic variations within Earths subsurface and the nature of the forcing (both frequency and stress) for GIA-related processes. We have adopted two simple plate models for Western Antarctica and the Antarctic Peninsular and have self-consistently determined their full spectrum mechanical behavior. We have applied a means of assessing the frequency contents of observational results so that these observationally derived apparent quantities may be compared to prediction.

While our modeling of the subsurface structure is highly simplified, we have demonstrated that our current understanding of Earth deformation, derived from microphysical investigations that operate on timescales appropriate for the laboratory setting, shows significant promise in explaining some of the variability we observe on the planetary scale and across timescales that capture Earth's long and nuanced history. Looking to the future, we envision both the inclusion of viscoelastic models in GIA that move beyond the Maxwell model (e.g., Peltier et al., 1980; Chanard et al., 2018; Ivins et al., 2020), the determination of the frequency content within measurements of time-domain processes like GIA, and the search to map out the continuous function $\tilde{\eta}(\omega)$, rather than discrete values of η_0, to help improve predictions of cryosphere-solid Earth responses as rates of ice sheet melting and collapse increasingly occur on shorter timescales.

Appendix A Stress Evolution during GIA

To demonstrate the stress levels that can be reached in the uppermost upper mantle, we perform a simple viscoelastic loading calculation adopting a Maxwell viscoelastic model. We use the formulation of Mitrovica and Milne (2003) though with simplifications: we assume longitudinal symmetry, no rotation, and that we only calculate solid earth deformation in response to ice growth (i.e., we do not consider the effects of the ocean); and thus, only focus on the vicinity of the ice sheet. The input parameters include the elastic and density profile of PREM (Dziewonski & Anderson, 1981). We impose a lithosphere of 200 km thickness and values of η_0 of 5×10^{20} Pa s and 5×10^{21} Pa s across the upper mantle (200 to 670 km depth) and lower mantle (670 to 2900 km depth), respectively. The growth of an ice sheet of 1,000 m over ∼5,000 years results in stress levels within the lithosphere and asthenosphere that reach ∼MPa – sufficient to induce changes in dislocation structure. The results are summarized in Fig. A1.

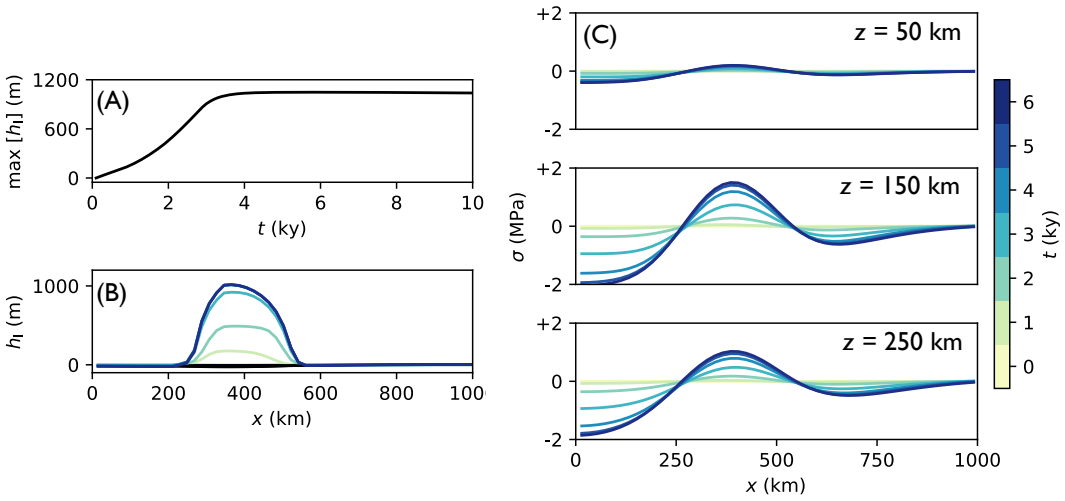

Figure A1. Stress Evolution During GIA. (A) Maximum ice height as a function of time. (B) Ice profiles as a function of distance from the North Pole (x). Each line represents the profile at a given time indicated by the colorbar. The solid black lines are the associated bedrock elevations. (c) The stress profiles at different depth, z, slices, as a function of x. Each line represents the stress profile at a given time indicated by the color bar.

Appendix B Timescales Assigned to Observations

Reference	Region	τ_{dur}; τ_{del}	Comment
Whitehouse et al. (2012)	ASE	15,000 y; 0 y	Investigation last glacial maximum with relative sea level data.
Barletta et al. (2018)	ASE	102 y and 12 y; 0 y	Ice change in the Amundsen Bay region with two rates of ice loss between 1900-2002 and 2002-2014, measured from 2002 onwards.
Wolstencroft et al. (2015)	AP	15,000 y 5,000 y	Last glacial maximum, 21,000 y BP, to 6,000 y BP with deformation measured by GPS today.
Ivins et al. (2011)	AP	200 y and 80 y; 700 y and 70 y	Deformation from the Little Ice Age (1030 CE1300 CE) and modern ice mass change (18501930) recorded by GPS over a duration of 1993-2007.
Nield et al. (2014)	AP	10 y; 7 y	Collapse of Larsen B ice shelf between 1993-2002, recorded by GPS stations from 2009.
Samrat et al. (2020)	AP	15 y; 7 y	Ice mass loss of Larsen A and B ice shelves measured by GPS extended to up to 2018 from Nield et al. (2014).

Table B1. Tabulation of all the assigned values of τ_{dur} and τ_{del} for each observation and the associated explanation. For each value of τ_{dur} andτ_{del} listed, we consider $\pm 20\%$ of these values also.

Acknowledgments

HL acknowledges support from UC Berkeley. The VBRc is available for download at DOI:10.5281/zenodo.4317820. We thank the two anonymous reviewers who greatly improved the manuscript.

References

An, M., Wiens, D. A., Zhao, Y., Feng, M., Nyblade, A., Kanao, M., ... Lévêque, J.-J. (2015, December). Temperature, lithosphere-asthenosphere boundary, and heat flux beneath the Antarctic Plate inferred from seismic velocities.

Journal of Geophysical Research (Solid Earth), *120*(12), 8720-8742. doi: 10.1002/2015JB011917

An, M., Wiens, D. A., Zhao, Y., Feng, M., Nyblade, A. A., Kanao, M., ... Lévêque, J.-J. (2015, January). S -velocity model and inferred moho topography beneath the antarctic plate from rayleigh waves. *Journal of Geophysical Research: Solid Earth*, *120*(1), 359–383. Retrieved from `https://doi.org/10.1002/2014jb011332` doi: 10.1002/2014jb011332

Andrade, E. N. D. C. (1910, June). On the Viscous Flow in Metals, and Allied Phenomena. *Proceedings of the Royal Society of London Series A*, *84*(567), 1-12.

Austermann, J., Chen, C. Y., Lau, H. C., Maloof, A. C., & Latychev, K. (2020, feb). Constraints on mantle viscosity and Laurentide ice sheet evolution from pluvial paleolake shorelines in the western United States. *Earth and Planetary Science Letters*, *532*, 116006. doi: 10.1016/j.epsl.2019.116006

Austermann, J., Hoggard, M., & Mitrovica, J. (2021, October). fill in properly... *in revision*, *1*(9), e1500360-e1500360. doi: 10.1126/sciadv.1500360

Barletta, V. R., Bevis, M., Smith, B. E., Wilson, T., Brown, A., Bordoni, A., ... Wiens, D. A. (2018, jun). Observed rapid bedrock uplift in amundsen sea embayment promotes ice-sheet stability. *Science*, *360*(6395), 1335–1339. doi: 10.1126/science.aao1447

Benjamin, D., Wahr, J., Ray, R. D., Egbert, G. D., & Desai, S. D. (2006, April). Constraints on mantle anelasticity from geodetic observations, and implications for the J 2 anomaly. *Geophysical Journal International*, *165*(1), 3–16. doi: 10.1111/j.1365-246X.2006.02915.x

Berman, R. G., & Aranovich, L. Y. (1996, December). Optimized standard state and solution properties of minerals ¡SBT¿I. Model calibration for olivine, orthopyroxene, cordierite, garnet, and ilmenite in the system FeO-MgO-CaO-Al_2O_3-TiO_2-SiO_2¡/SBT¿. *Contributions to Mineralogy and Petrology*, *126*, 1-24. doi: 10.1007/s004100050232

Cammarano, F., Goes, S., Vacher, P., & Giardini, D. (2003, August). Inferring upper-mantle temperatures from seismic velocities. *Physics of the Earth and Planetary Interiors*, *138*(3-4), 197-222. doi: 10.1016/S0031-9201(03)00156-0

Caron, L., Mtivier, L., Greff-Lefftz, M., Fleitout, L., & Rouby, H. (2017, 02). Inverting Glacial Isostatic Adjustment signal using Bayesian framework and two linearly relaxing rheologies. *Geophysical Journal International*, *209*(2), 1126-1147. Retrieved from `https://doi.org/10.1093/gji/ggx083` doi: 10.1093/gji/ggx083

Chanard, K., Fleitout, L., Calais, E., Barbot, S., & Avouac, J.-P. (2018, March). Constraints on Transient Viscoelastic Rheology of the Asthenosphere From Seasonal Deformation. *Geophysical Research Letters*, *45*(5), 2328-2338. doi: 10.1002/2017GL076451

Chen, B., Haeger, C., Kaban, M. K., & Petrunin, A. G. (2018). Variations of the effective elastic thickness reveal tectonic fragmentation of the antarctic lithosphere. *Tectonophysics*, *746*, 412-424. Retrieved from `https://www.sciencedirect.com/science/article/pii/S0040195117302573` (Understanding geological processes through modelling - A Memorial Volume honouring Evgenii Burov) doi: https://doi.org/10.1016/j.tecto.2017.06.012

Conrad, C. P., & Lithgow-Bertelloni, C. (2006, March). Influence of continental roots and asthenosphere on plate-mantle coupling. , *33*(5), L05312. doi: 10.1029/2005GL025621

Cooper, R. F. (2002, January). Seismic Wave Attenuation: Energy Dissipation in Viscoelastic Crystalline Solids. *Reviews in Mineralogy and Geochemistry*, *51*, 253-290. doi: 10.2138/gsrmg.51.1.253

Cooper, R. F., Stone, D. S., & Plookphol, T. (2016, October). Load relaxation of olivine single crystals. *Journal of Geophysical Research (Solid Earth)*, *121*(10), 7193-7210. doi: 10.1002/2016JB013425

Crawford, O., Al-Attar, D., Tromp, J., Mitrovica, J. X., Austermann, J., & Lau, H. C. P. (2018, August). Quantifying the sensitivity of post-glacial sea level change to laterally varying viscosity. *Geophysical Journal International*, *214*(2), 1324-1363. doi: 10.1093/gji/ggy184

Duffy, T. S., & Anderson, D. L. (1989, February). Seismic velocities in mantle minerals and the mineralogy of the upper mantle. *Journal of Geophysical Research*, *94*, 1895-1912. doi: 10.1029/JB094iB02p01895

Dziewonski, A. M., & Anderson, D. L. (1981, June). Preliminary reference Earth model. *Physics of the Earth and Planetary Interiors*, *25*(4), 297–356. doi: 10.1016/0031-9201(81)90046-7

Farla, R. J. M., Jackson, I., Fitz Gerald, J. D., Faul, U. H., & Zimmerman, M. E. (2012, April). Dislocation Damping and Anisotropic Seismic Wave Attenuation in Earth's Upper Mantle. *Science*, *336*, 332. doi: 10.1126/science.1218318

Faul, U., & Jackson, I. (2015, May). Transient Creep and Strain Energy Dissipation: An Experimental Perspective. *Annual Review of Earth and Planetary Sciences*, *43*(1), 541–569. Retrieved from `http://www.annualreviews.org/doi/abs/10.1146/annurev-earth-060313-054732` doi: 10.1146/annurev-earth-060313-054732

Faul, U. H., Fitz Gerald, J. D., & Jackson, I. (2004, June). Shear wave attenuation and dispersion in melt-bearing olivine polycrystals: 2. Microstructural interpretation and seismological implications. *Journal of Geophysical Research (Solid Earth)*, *109*(B6), B06202. doi: 10.1029/2003JB002407

Fischer, K. M., Ford, H. A., Abt, D. L., & Rychert, C. A. (2010, May). The Lithosphere-Asthenosphere Boundary. *Annual Review of Earth and Planetary Sciences*, *38*(1), 551-575. doi: 10.1146/annurev-earth-040809-152438

Goes, S., Govers, R., & Vacher, P. (2000, May). Shallow mantle temperatures under Europe from P and S wave tomography. *Journal of Geophysical Research*, *105*(B5), 11,153-11,169. doi: 10.1029/1999JB900300

Goes, S., & van der Lee, S. (2002, March). Thermal structure of the North American uppermost mantle inferred from seismic tomography. *Journal of Geophysical Research (Solid Earth)*, *107*(B3), 2050. doi: 10.1029/2000JB000049

Goldberg, S. L., Lau, H. C. P., Mitrovica, J. X., & Latychev, K. (2016, October). The timing of the Black Sea flood event: Insights from modeling of glacial isostatic adjustment. *Earth and Planetary Science Letters*, *452*, 178-184. doi: 10.1016/j.epsl.2016.06.016

Gomez, N., Mitrovica, J. X., Huybers, P., & Clark, P. U. (2010, December). Sea level as a stabilizing factor for marine-ice-sheet grounding lines. *Nature Geoscience*, *3*(12), 850-853. doi: 10.1038/ngeo1012

Gribb, T. T., & Cooper, R. F. (1998, November). Low-frequency shear attenuation in polycrystalline olivine: Grain boundary diffusion and the physical significance of the Andrade model for viscoelastic rheology. *Journal of Geophysical Research: Solid Earth*, *103*(B11), 27267–27279. Retrieved from `http://doi.wiley.com/10.1029/98JB02786` doi: 10.1029/98JB02786

Gribb, T. T., & Cooper, R. F. (2000, August). The effect of an equilibrated melt phase on the shear creep and attenuation behavior of polycrystalline olivine. *Geophysical Research Letters*, *27*(15), 2341-2344. doi: 10.1029/2000GL011443

Gunasekaran, S., & Ak, M. (2002). *Cheese rheology and texture*. CRC Press. Retrieved from `https://books.google.com/books?id=KBzNBQAAQBAJ`

Haines, G. V., & Jones, A. G. (1988, January). Logarithmic Fourier transformation. *Geophysical Journal International*, *92*(1), 171-178. doi: 10.1111/j.1365-246X.1988.tb01131.x

Hammond, W. C., & Humphreys, E. D. (2000, May). Upper mantle seismic wave velocity: Effects of realistic partial melt geometries. *Journal of Geophysical Research*, *105*, 10. doi: 10.1029/2000JB900041

Hansen, L. N., Kumamoto, K. M., Thom, C. A., Wallis, D., Durham, W. B.,

Goldsby, D. L., ... Kohlstedt, D. L. (2019). Low-temperature plasticity in olivine: Grain size, strain hardening, and the strength of the lithosphere. *Journal of Geophysical Research: Solid Earth*, *0*(ja). Retrieved from https://agupubs.onlinelibrary.wiley.com/doi/abs/10.1029/2018JB016736 doi: 10.1029/2018JB016736

Hansen, L. N., Zimmerman, M. E., & Kohlstedt, D. L. (2011). Grain boundary sliding in san carlos olivine: Flow law parameters and crystallographic-preferred orientation. *Journal of Geophysical Research: Solid Earth*, *116*(B8).

Haskell, N. A. (1935, August). The Motion of a Viscous Fluid Under a Surface Load. *Physics*, *6*(8), 265-269. doi: 10.1063/1.1745329

Havlin, C., Holtzman, B. K., & Hopper, E. (2021). Inference of thermodynamic state in the asthenosphere from anelastic properties, with applications to north american upper mantle. *Physics of the Earth and Planetary Interiors*, *314*, 106639. Retrieved from https://www.sciencedirect.com/science/article/pii/S003192012030399X doi: https://doi.org/10.1016/j.pepi.2020.106639

Hay, C. C., Lau, H. C. P., Gomez, N., Austermann, J., Powell, E., Mitrovica, J. X., ... Wiens, D. A. (2017, March). Sea Level Fingerprints in a Region of Complex Earth Structure: The Case of WAIS. *Journal of Climate*, *30*(6), 1881-1892. doi: 10.1175/JCLI-D-16-0388.1

Hirth, G., & Kohlstedt, D. (2003). Rheology of the upper mantle and the mantle wedge: A view from the experimentalists. *Washington DC American Geophysical Union Geophysical Monograph Series*, *138*, 83-105. doi: 10.1029/138GM06

Hopper, E., & Fischer, K. M. (2018, August). The Changing Face of the Lithosphere-Asthenosphere Boundary: Imaging Continental Scale Patterns in Upper Mantle Structure Across the Contiguous U.S. With Sp Converted Waves. *Geochemistry, Geophysics, Geosystems*, *19*(8), 2593-2614. doi: 10.1029/2018GC007476

Huang, P., Wu, P., & Steffen, H. (2019, July). In search of an ice history that is consistent with composite rheology in Glacial Isostatic Adjustment modelling. *Earth and Planetary Science Letters*, *517*, 26-37. doi: 10.1016/j.epsl.2019.04.011

Isaak, D. G. (1992, February). High-temperature elasticity of iron-bearing olivines. *Journal of Geophysical Research*, *97*(B2), 1871-1885. doi: 10.1029/91JB02675

Ivins, E. R., Caron, L., Adhikari, S., Larour, E., & Scheinert, M. (2020, October). A linear viscoelasticity for decadal to centennial time scale mantle deformation. *Reports on Progress in Physics*, *83*(10), 106801. doi: 10.1088/1361-6633/aba346

Ivins, E. R., Watkins, M. M., Yuan, D. N., Dietrich, R., Casassa, G., & Rülke, A. (2011, feb). On-land ice loss and glacial isostatic adjustment at the Drake Passage: 2003-2009. *Journal of Geophysical Research: Solid Earth*, *116*(2). doi: 10.1029/2010JB007607

Jackson, I., & Faul, U. H. (2010, November). Grainsize-sensitive viscoelastic relaxation in olivine: Towards a robust laboratory-based model for seismological application. *Physics of the Earth and Planetary Interiors*, *183*(1-2), 151–163. Retrieved from http://www.sciencedirect.com/science/article/pii/S0031920110001871 doi: 10.1016/j.pepi.2010.09.005

Jackson, I., Faul, U. H., Fitz Gerald, J. D., & Tan, B. H. (2004, June). Shear wave attenuation and dispersion in melt-bearing olivine polycrystals: 1. Specimen fabrication and mechanical testing. *Journal of Geophysical Research (Solid Earth)*, *109*(B6), B06201. doi: 10.1029/2003JB002406

Jackson, I., Faul, U. H., Gerald, J. D. F., & Morris, S. (2006). Contrasting viscoelastic behavior of melt-free and melt-bearing olivine: Implications for the nature of grain-boundary sliding. *Materials Science and Engineering: A*, *442*(1), 170-174. Retrieved from https://www.sciencedirect.com/

science/article/pii/S0921509306010938 (Proceedings of the 14th International Conference on Internal Friction and Mechanical Spectroscopy) doi: https://doi.org/10.1016/j.msea.2006.01.136

Kanamori, H., & Anderson, D. L. (1977). Importance of physical dispersion in surface wave and free oscillation problems: Review. *Reviews of Geophysics*, *15*(1), 105. Retrieved from http://doi.wiley.com/10.1029/RG015i001p00105 doi: 10.1029/RG015i001p00105

Karato, S.-I., & Wu, P. (1993, May). Rheology of the Upper Mantle: A Synthesis. *Science*, *260*(5109), 771-778. doi: 10.1126/science.260.5109.771

Kaufmann, G., Wu, P., & Ivins, E. R. (2005, March). Lateral viscosity variations beneath Antarctica and their implications on regional rebound motions and seismotectonics. *Journal of Geodynamics*, *39*(2), 165-181. doi: 10.1016/j.jog.2004.08.009

Khan, A., Boschi, L., & Connolly, J. (2009, June). On mantle chemical and thermal heterogeneities and anisotropy as mapped by inversion of global surface wave data. *Geochimica et Cosmochimica Acta Supplement*, *73*, A645.

King, M. A., & Santamaría-Gómez, A. (2016, March). Ongoing deformation of Antarctica following recent Great Earthquakes. *Geophysical Research Letters*, *43*(5), 1918-1927. doi: 10.1002/2016GL067773

Kumazawa, M., & Anderson, O. L. (1969, November). Elastic moduli, pressure derivatives, and temperature derivatives of single-crystal olivine and single-crystal forsterite. *Journal of Geophysical Research*, *74*(25), 5961-5972. doi: 10.1029/JB074i025p05961

Larour, E., Seroussi, H., Adhikari, S., Ivins, E., Caron, L., Morlighem, M., & Schlegel, N. (2019, jun). Slowdown in Antarctic mass loss from solid Earth and sea-level feedbacks. *Science*, *364*(6444). doi: 10.1126/science.aav7908

Latychev, K., Mitrovica, J. X., Tromp, J., Tamisiea, M. E., Komatitsch, D., & Christara, C. C. (2005, 05). Glacial isostatic adjustment on 3-D Earth models: a finite-volume formulation. *Geophysical Journal International*, *161*(2), 421-444. Retrieved from https://doi.org/10.1111/j.1365-246X.2005.02536.x doi: 10.1111/j.1365-246X.2005.02536.x

Lau, H. C. P., Faul, U., Mitrovica, J. X., Al-Attar, D., Tromp, J., & Garapić, G. (2017, January). Anelasticity across seismic to tidal timescales: a self-consistent approach. *Geophysical Journal International*, *208*, 368-384. doi: 10.1093/gji/ggw401

Lau, H. C. P., & Faul, U. H. (2019, February). Anelasticity from seismic to tidal timescales: Theory and observations. *Earth and Planetary Science Letters*, *508*, 18-29. doi: 10.1016/j.epsl.2018.12.009

Lau, H. C. P., & Holtzman, B. K. (2019, August). "Measures of Dissipation in Viscoelastic Media" Extended: Toward Continuous Characterization Across Very Broad Geophysical Time Scales. *Geophysical Research Letters*, *46*(16), 9544-9553. doi: 10.1029/2019GL083529

Lau, H. C. P., Holtzman, B. K., & Havlin, C. (2020). Toward a self-consistent characterization of lithospheric plates using full-spectrum viscoelasticity. *AGU Advances*, *1*(4), e2020AV000205. Retrieved from https://agupubs.onlinelibrary.wiley.com/doi/abs/10.1029/2020AV000205 (e2020AV000205 10.1029/2020AV000205) doi: https://doi.org/10.1029/2020AV000205

Lekić, V., Matas, J., Panning, M., & Romanowicz, B. (2009, May). Measurement and implications of frequency dependence of attenuation. *Earth and Planetary Science Letters*, *282*(1-4), 285–293. Retrieved from http://www.sciencedirect.com/science/article/pii/S0012821X09001800 doi: 10.1016/j.epsl.2009.03.030

Lloyd, A., Wiens, D., Zhu, H., Tromp, J., Nyblade, A., Aster, R., ... O'Donnell, J. (2019, oct). Seismic Structure of the Antarctic Upper Mantle Based on

Adjoint Tomography. *Journal of Geophysical Research: Solid Earth*. doi: 10.1029/2019jb017823

Mancinelli, N. J., Fischer, K. M., & Dalton, C. A. (2017, October). How Sharp Is the Cratonic Lithosphere-Asthenosphere Transition? *Geophysical Research Letters*, *44*(20), 10,189-10,197. doi: 10.1002/2017GL074518

McCarthy, C., Takei, Y., & Hiraga, T. (2011, September). Experimental study of attenuation and dispersion over a broad frequency range: 2. The universal scaling of polycrystalline materials. *Journal of Geophysical Research*, *116*(B9), B09207. Retrieved from `http://doi.wiley.com/10.1029/2011JB008384` doi: 10.1029/2011JB008384

Minster, J. B., & Anderson, D. L. (1980, November). Dislocations and nonelastic processes in the mantle. *Journal of Geophysical Research*, *85*(B11), 6347-6352. doi: 10.1029/JB085iB11p06347

Mitrovica, J. X., & Milne, G. A. (2003, 08). On post-glacial sea level: I. General theory. *Geophysical Journal International*, *154*(2), 253-267. Retrieved from `https://doi.org/10.1046/j.1365-246X.2003.01942.x` doi: 10.1046/j.1365-246X.2003.01942.x

Morris, S., & Jackson, I. (2009, April). Diffusionally assisted grain-boundary sliding and viscoelasticity of polycrystals. *Journal of the Mechanics and Physics of Solids*, *57*(4), 744–761. Retrieved from `http://www.sciencedirect.com/science/article/pii/S0022509608002263` doi: 10.1016/j.jmps.2008.12.006

Nakada, M., & Lambeck, K. (1989, March). Late Pleistocene and Holocene sea-level change in the Australian region and mantle rheology. *Geophysical Journal International*, *96*(3), 497-517. doi: 10.1111/j.1365-246X.1989.tb06010.x

Nield, G. A., Barletta, V. R., Bordoni, A., King, M. A., Whitehouse, P. L., Clarke, P. J., ... Berthier, E. (2014). Rapid bedrock uplift in the antarctic peninsula explained by viscoelastic response to recent ice unloading. *Earth and Planetary Science Letters*, *397*, 32-41. Retrieved from `https://www.sciencedirect.com/science/article/pii/S0012821X14002519` doi: https://doi.org/10.1016/j.epsl.2014.04.019

Nield, G. A., Whitehouse, P. L., King, M. A., & Clarke, P. J. (2016, April). Glacial isostatic adjustment in response to changing Late Holocene behaviour of ice streams on the Siple Coast, West Antarctica. *Geophysical Journal International*, *205*(1), 1-21. doi: 10.1093/gji/ggv532

Nield, G. A., Whitehouse, P. L., vanÂ derÂ Wal, W., Blank, B., O'Donnell, J. P., & Stuart, G. W. (2018, August). The impact of lateral variations in lithospheric thickness on glacial isostatic adjustment in West Antarctica. *Geophysical Journal International*, *214*(2), 811-824. doi: 10.1093/gji/ggy158

Nowick, A., & Berry, B. (1972). *Anelastic relaxation in crystalline materials*. New York: Academic.

O'Connell, R. J., & Budiansky, B. (1977, December). Viscoelastic properties of fluid-saturated cracked solids. *Journal of Geophysical Research*, *82*, 5719-5735. doi: 10.1029/JB082i036p05719

O'Donnell, J., Selway, K., Nyblade, A., Brazier, R., Wiens, D., Anandakrishnan, S., ... Winberry, J. (2017). The uppermost mantle seismic velocity and viscosity structure of central west antarctica. *Earth and Planetary Science Letters*, *472*, 38-49. Retrieved from `https://www.sciencedirect.com/science/article/pii/S0012821X17302765` doi: https://doi.org/10.1016/j.epsl.2017.05.016

Ohuchi, T., Kawazoe, T., Higo, Y., Funakoshi, K. i., Suzuki, A., Kikegawa, T., & Irifune, T. (2015, October). Dislocation-accommodated grain boundary sliding as the major deformation mechanism of olivine in the Earth's upper mantle. *Science Advances*, *1*(9), e1500360-e1500360. doi: 10.1126/sciadv.1500360

Pan, L., Powell, E. M., Latychev, K., Mitrovica, J. X., Creveling, J. R., Gomez, N., ... Clark, P. U. (2021). Rapid postglacial rebound amplifies global sea level rise following west antarctic ice sheet collapse. *Science Advances*, *7*(18). Re-

trieved from https://advances.sciencemag.org/content/7/18/eabf7787 doi: 10.1126/sciadv.abf7787

Peltier, W. R., & Andrews, J. T. (1976). Glacial-isostatic adjustmenti. the forward problem. *Geophysical Journal of the Royal Astronomical Society*, *46*(3), 605-646. Retrieved from https://onlinelibrary.wiley.com/doi/abs/10.1111/j.1365-246X.1976.tb01251.x doi: 10.1111/j.1365-246X.1976.tb01251.x

Peltier, W. R., Yuen, D. A., & Wu, P. (1980). Postglacial rebound and transient rheology. *Geophysical Research Letters*, *7*, 733-736. doi: 10.1029/GL007i010p00733

Powell, E., Gomez, N., Hay, C., Latychev, K., & Mitrovica, J. X. (2020, January). Viscous Effects in the Solid Earth Response to Modern Antarctic Ice Mass Flux: Implications for Geodetic Studies of WAIS Stability in a Warming World. *Journal of Climate*, *33*(2), 443-459. doi: 10.1175/JCLI-D-19-0479.1

Raj, R. (1975, August). Transient behavior of diffusion-induced creep and creep rupture. *Metallurgical Transactions A*, *6*(8), 1499–1509. Retrieved from http://link.springer.com/10.1007/BF02641961 doi: 10.1007/BF02641961

Raj, R., & Ashby, M. F. (1971, April). On grain boundary sliding and diffusional creep. *Metallurgical Transactions*, *2*(4), 1113–1127. Retrieved from http://link.springer.com/10.1007/BF02664244 doi: 10.1007/BF02664244

Richards, F. D., Hoggard, M. J., White, N., & Ghelichkhan, S. (2020, September). Quantifying the Relationship Between Short-Wavelength Dynamic Topography and Thermomechanical Structure of the Upper Mantle Using Calibrated Parameterization of Anelasticity. *Journal of Geophysical Research (Solid Earth)*, *125*(9), e19062. doi: 10.1029/2019JB019062

Samrat, N. H., King, M. A., Watson, C., Hooper, A., Chen, X., Barletta, V. R., & Bordoni, A. (2020, may). Reduced ice mass loss and three-dimensional viscoelastic deformation in northern Antarctic Peninsula inferred from GPS. *Geophysical Journal International*, *222*(2), 1013–1022. Retrieved from https://doi.org/10.1093/gji/ggaa229 doi: 10.1093/gji/ggaa229

Sasaki, Y., Takei, Y., McCarthy, C., & Rudge, J. F. (2019). Experimental study of dislocation damping using a rock analogue. *Journal of Geophysical Research: Solid Earth*, *124*(7), 6523-6541. Retrieved from https://agupubs.onlinelibrary.wiley.com/doi/abs/10.1029/2018JB016906 doi: https://doi.org/10.1029/2018JB016906

Sella, G. F., Stein, S., Dixon, T. H., Craymer, M., James, T. S., Mazzotti, S., & Dokka, R. K. (2007, jan). Observation of glacial isostatic adjustment in stable North America with GPS. *Geophysical Research Letters*, *34*(2), L02306. Retrieved from http://doi.wiley.com/10.1029/2006GL027081 doi: 10.1029/2006GL027081

Shito, A., Karato, S.-i., & Park, J. (2004, June). Frequency dependence of Q in Earth's upper mantle inferred from continuous spectra of body waves. *Geophysical Research Letters*, *31*(12), n/a–n/a. Retrieved from http://doi.wiley.com/10.1029/2004GL019582 doi: 10.1029/2004GL019582

Spada, G. (2017, January). Glacial Isostatic Adjustment and Contemporary Sea Level Rise: An Overview. *Surveys in Geophysics*, *38*(1), 153-185. doi: 10.1007/s10712-016-9379-x

Stixrude, L. (2007, 12). Properties of rocks and minerals seismic properties of rocks and minerals, and structure of the earth. In (Vol. 2, p. 7-32). doi: 10.1016/B978-044452748-6.00042-0

Stixrude, L., & Lithgow-Bertelloni, C. (2005, August). Thermodynamics of mantle minerals - I. Physical properties. *Geophysical Journal International*, *162*, 610-632. doi: 10.1111/j.1365-246X.2005.02642.x

Sundberg, M., & Cooper, R. F. (2010, July). A composite viscoelastic model for incorporating grain boundary sliding and transient diffusion creep; correlating creep and attenuation responses for materials with a fine grain size. *Philosoph-*

ical Magazine, *90*, 2817-2840. doi: 10.1080/14786431003746656

Takei, Y. (1998, August). Constitutive mechanical relations of solid-liquid composites in terms of grain-boundary contiguity. *Journal of Geophysical Research*, *103*(B8), 18,183-18,203. doi: 10.1029/98JB01489

Takei, Y. (2002, February). Effect of pore geometry on V_P/V_S: From equilibrium geometry to crack. *Journal of Geophysical Research (Solid Earth)*, *107*(B2), 2043. doi: 10.1029/2001JB000522

Takei, Y. (2017, August). Effects of Partial Melting on Seismic Velocity and Attenuation: A New Insight from Experiments. *Annual Review of Earth and Planetary Sciences*, *45*, 447-470. doi: 10.1146/annurev-earth-063016-015820

Thieme, M., Demouchy, S., Mainprice, D., Barou, F., & Cordier, P. (2018, May). Stress evolution and associated microstructure during transient creep of olivine at 1000-1200 °C. *Physics of the Earth and Planetary Interiors*, *278*, 34-46. doi: 10.1016/j.pepi.2018.03.002

van der Wal, W., Barnhoorn, A., Stocchi, P., Gradmann, S., Wu, P., Drury, M., & Vermeersen, B. (2013, July). Glacial isostatic adjustment model with composite 3-D Earth rheology for Fennoscandia. *Geophysical Journal International*, *194*(1), 61-77. doi: 10.1093/gji/ggt099

van der Wal, W., Whitehouse, P. L., & Schrama, E. J. O. (2015, March). Effect of GIA models with 3D composite mantle viscosity on GRACE mass balance estimates for Antarctica. *Earth and Planetary Science Letters*, *414*, 134-143. doi: 10.1016/j.epsl.2015.01.001

van der Wal, W., Wu, P., Wang, H., & Sideris, M. G. (2010, July). Sea levels and uplift rate from composite rheology in glacial isostatic adjustment modeling. *Journal of Geodynamics*, *50*(1), 38-48. doi: 10.1016/j.jog.2010.01.006

Watts, A. B., Zhong, S. J., & Hunter, J. (2013, May). The Behavior of the Lithosphere on Seismic to Geologic Timescales. *Annual Review of Earth and Planetary Sciences*, *41*, 443-468. doi: 10.1146/annurev-earth-042711-105457

Whitehouse, P. L. (2018, May). Glacial isostatic adjustment modelling: historical perspectives, recent advances, and future directions. *Earth Surface Dynamics*, *6*(2), 401-429. doi: 10.5194/esurf-6-401-2018

Whitehouse, P. L., Bentley, M. J., Milne, G. A., King, M. A., & Thomas, I. D. (2012, September). A new glacial isostatic adjustment model for Antarctica: calibrated and tested using observations of relative sea-level change and present-day uplift rates. *Geophysical Journal International*, *190*(3), 1464-1482. doi: 10.1111/j.1365-246X.2012.05557.x

Wolstencroft, M., King, M. A., Whitehouse, P. L., Bentley, M. J., Nield, G. A., King, E. C., ... Gunter, B. C. (2015, aug). Uplift rates from a new high-density GPS network in Palmer Land indicate significant late Holocene ice loss in the southwestern Weddell Sea. *Geophysical Journal International*, *203*(1), 737–754. doi: 10.1093/gji/ggv327

Wu, P. (1992, January). Deformation of an incompressible viscoelastic flat earth with powerlaw creep: a finite element approach. *Geophysical Journal International*, *108*(1), 35-51. doi: 10.1111/j.1365-246X.1992.tb00837.x

Wu, P., & Peltier, W. R. (1982, August). Viscous gravitational relaxation. *Geophysical Journal*, *70*(2), 435-485. doi: 10.1111/j.1365-246X.1982.tb04976.x

Wu, P., & van der Wal, W. (2003, June). Postglacial sealevels on a spherical, self-gravitating viscoelastic earth: effects of lateral viscosity variations in the upper mantle on the inference of viscosity contrasts in the lower mantle. *Earth and Planetary Science Letters*, *211*(1-2), 57-68. doi: 10.1016/S0012-821X(03)00199-7

Xu, Y., Zimmerman, M. E., & Kohlstedt, D. L. (2004). Deformation behavior of partially molten mantle rocks. In *Rheology and deformation of the lithosphere at continental margins* (pp. 284–310). Columbia University Press. Retrieved from `http://www.jstor.org/stable/10.7312/karn12738.14`

Yamauchi, H., & Takei, Y. (2016, November). Polycrystal anelasticity at near-solidus temperatures. *Journal of Geophysical Research (Solid Earth)*, *121*(11), 7790-7820. doi: 10.1002/2016JB013316

Zener, C. (1941, December). Theory of the Elasticity of Polycrystals with Viscous Grain Boundaries. *Physical Review*, *60*(12), 906-908. doi: 10.1103/PhysRev.60.906

Zhong, S., Paulson, A., & Wahr, J. (2003, 11). Three-dimensional finite-element modelling of Earths viscoelastic deformation: effects of lateral variations in lithospheric thickness. *Geophysical Journal International*, *155*(2), 679-695. Retrieved from `https://doi.org/10.1046/j.1365-246X.2003.02084.x` doi: 10.1046/j.1365-246X.2003.02084.x

Figure 1.

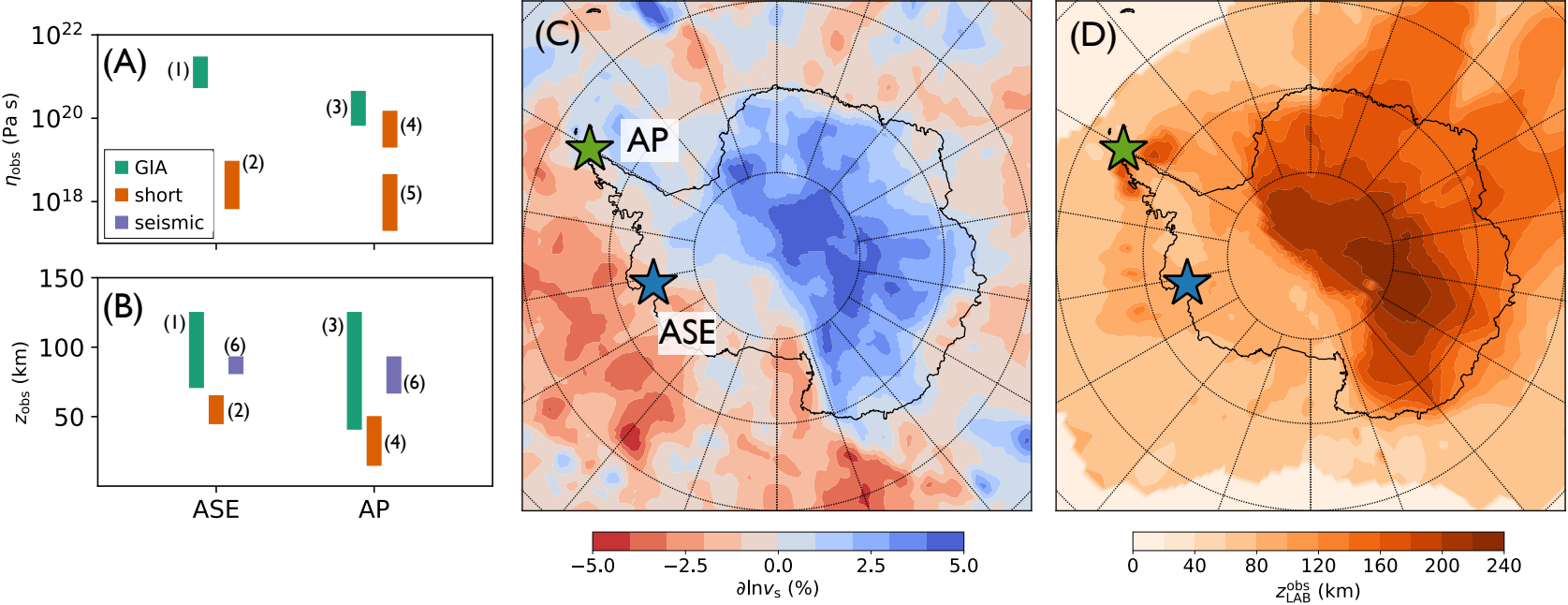
(A)
(I)
(2)
(3)
(4)
(5)
GIA
short
seismic
10^{22}
10^{20}
10^{18}
η_{obs} (Pa s)
(B)
(I)
(6)
(2)
(3)
(6)
(4)
150
100
50
z_{obs} (km)
ASE
AP
(C)
AP
ASE
−5.0
−2.5
0.0
2.5
5.0
$\partial \ln v_s$ (%)
(D)
0
40
80
120
160
200
240
z_{LAB}^{obs} (km)

Figure 2.

Arbitrary phenomenological model

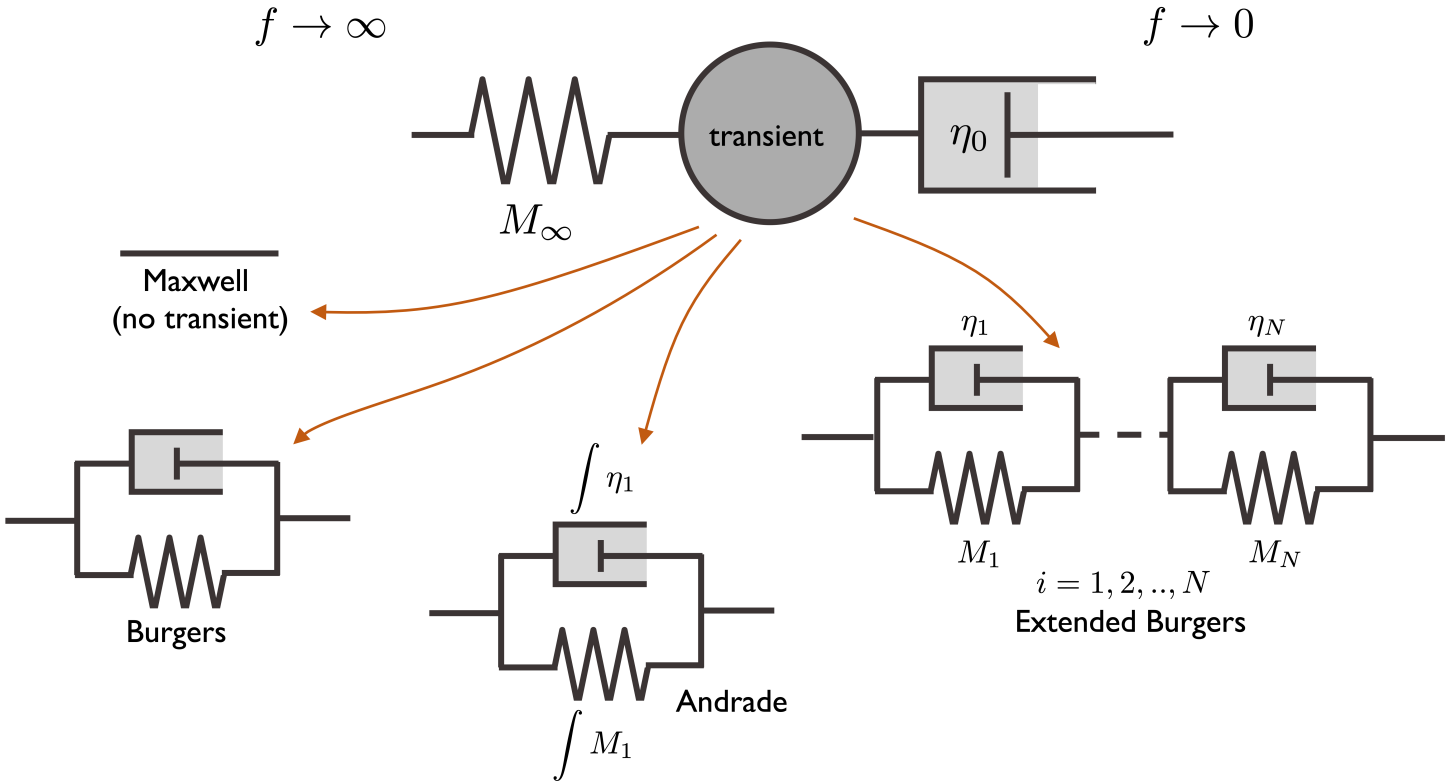

Addition of dislocation creep

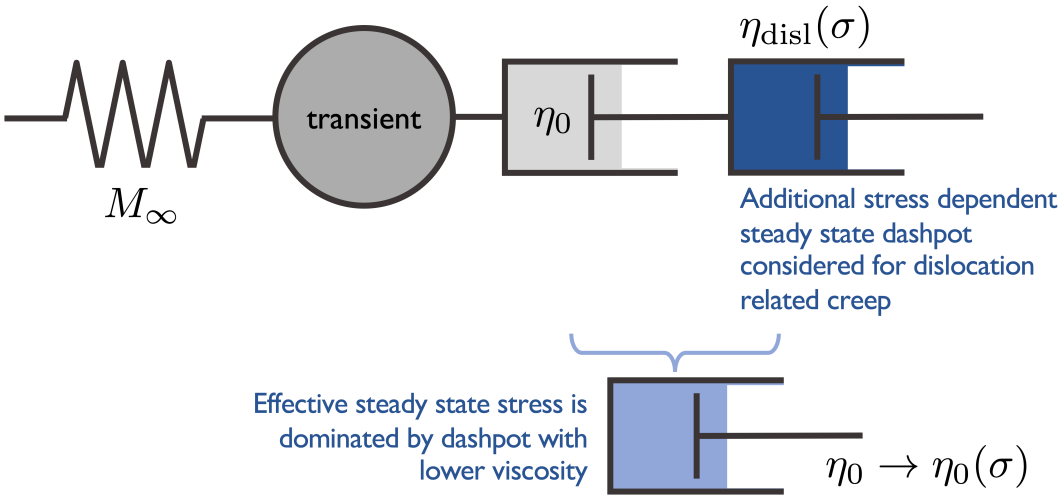

Figure 3.

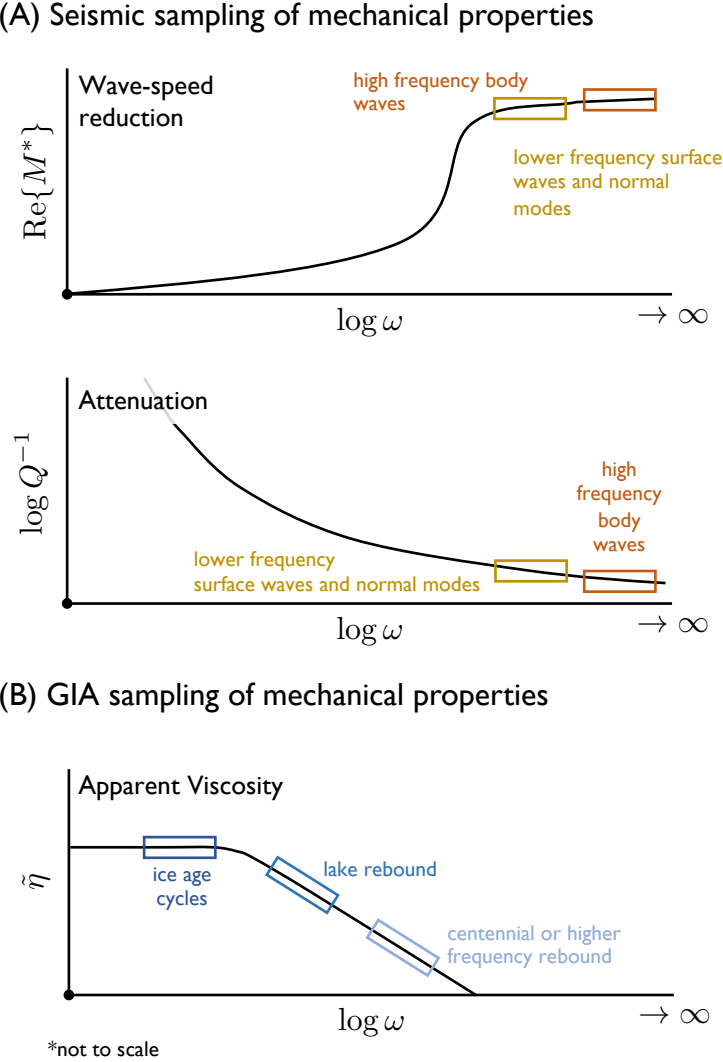
(A) Seismic sampling of mechanical properties
Wave-speed reduction
high frequency body waves
lower frequency surface waves and normal modes
$\mathrm{Re}\{M^*\}$
$\log \omega$
$\rightarrow \infty$
Attenuation
high frequency body waves
lower frequency surface waves and normal modes
$\log Q^{-1}$
$\log \omega$
$\rightarrow \infty$
(B) GIA sampling of mechanical properties
Apparent Viscosity
ice age cycles
lake rebound
centennial or higher frequency rebound
$\tilde{\eta}$
$\log \omega$
$\rightarrow \infty$
*not to scale

Figure 4.

(1) Produce many plate models

calculate for N plate models the thermodynamic variables, $\mathbf{S}_i|_{i=1,2,..,N}$, where $\mathbf{S}_i = [T_{\mathrm{P},i}, g_i, \phi_i, X_{\mathrm{H2O}}, X_{\mathrm{maj}}]$.

(2) Calculate synthetic observables for all plate models

Using $\mathbf{S}_i$ as input and the chosen constitutive law, the VBR calculator predicts N synthetic v_S profiles and values of $z_{\mathrm{LAB}}^{\mathrm{obs}}$ for each plate model at the frequency of observation.

(3) Find best fitting models

Extract v_S values from the synthetic profiles at the same depth window as observed v_S. Use the N synthetic v_S and z_{LAB} values in a Bayesian analysis against those extracted from seismic data. Produce the posterior probability distribution and select the best plate model $\mathbf{S}_{i=\mathrm{best}}$.

(4) Calculate full spectrum mechanical properties of best fitting plate model

Using laws from steady state flow, transient creep, and elastic deformation the VBR calculates the full spectrum mechanical properties for $\mathbf{S}_{i=\mathrm{best}}$ which includes parameters: M_∞, η_0, $Q^{-1}(f)$, $M^*(f)$

Figure 5.

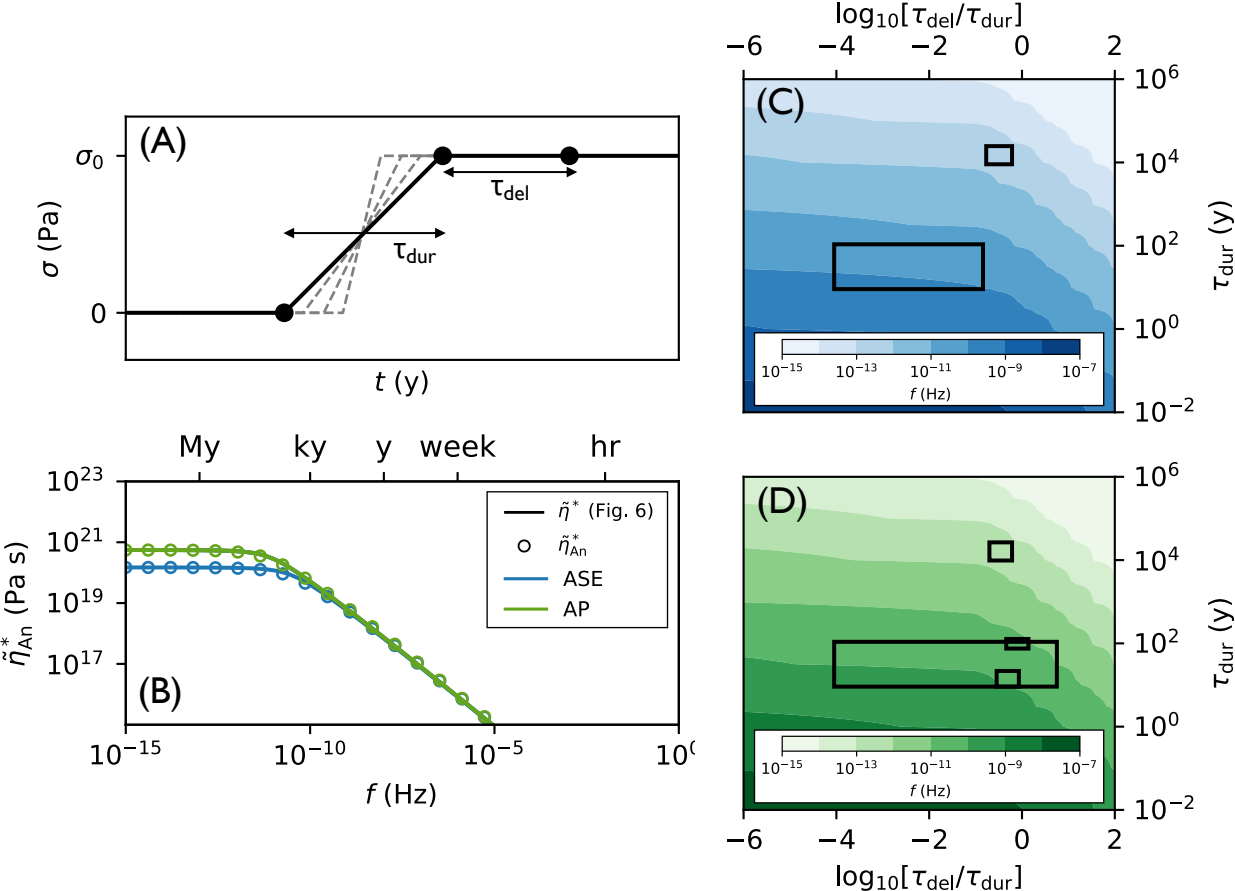
(A)
σ_0
0
σ (Pa)
τ_{del}
τ_{dur}
t (y)
My
ky
y
week
hr
10^{23}
10^{21}
10^{19}
10^{17}
$\tilde{\eta}^*_{An}$ (Pa s)
(B)
10^{-15}
10^{-10}
10^{-5}
f (Hz)
$\tilde{\eta}^*$ (Fig. 6)
$\tilde{\eta}^*_{An}$
ASE
AP
$\log_{10}[\tau_{del}/\tau_{dur}]$
−6
−4
−2
0
2
(C)
10^{6}
10^{4}
10^{2}
10^{0}
10^{-2}
τ_{dur} (y)
10^{-15}
10^{-13}
10^{-11}
10^{-9}
10^{-7}
f (Hz)
(D)
$\log_{10}[\tau_{del}/\tau_{dur}]$

Figure 6.

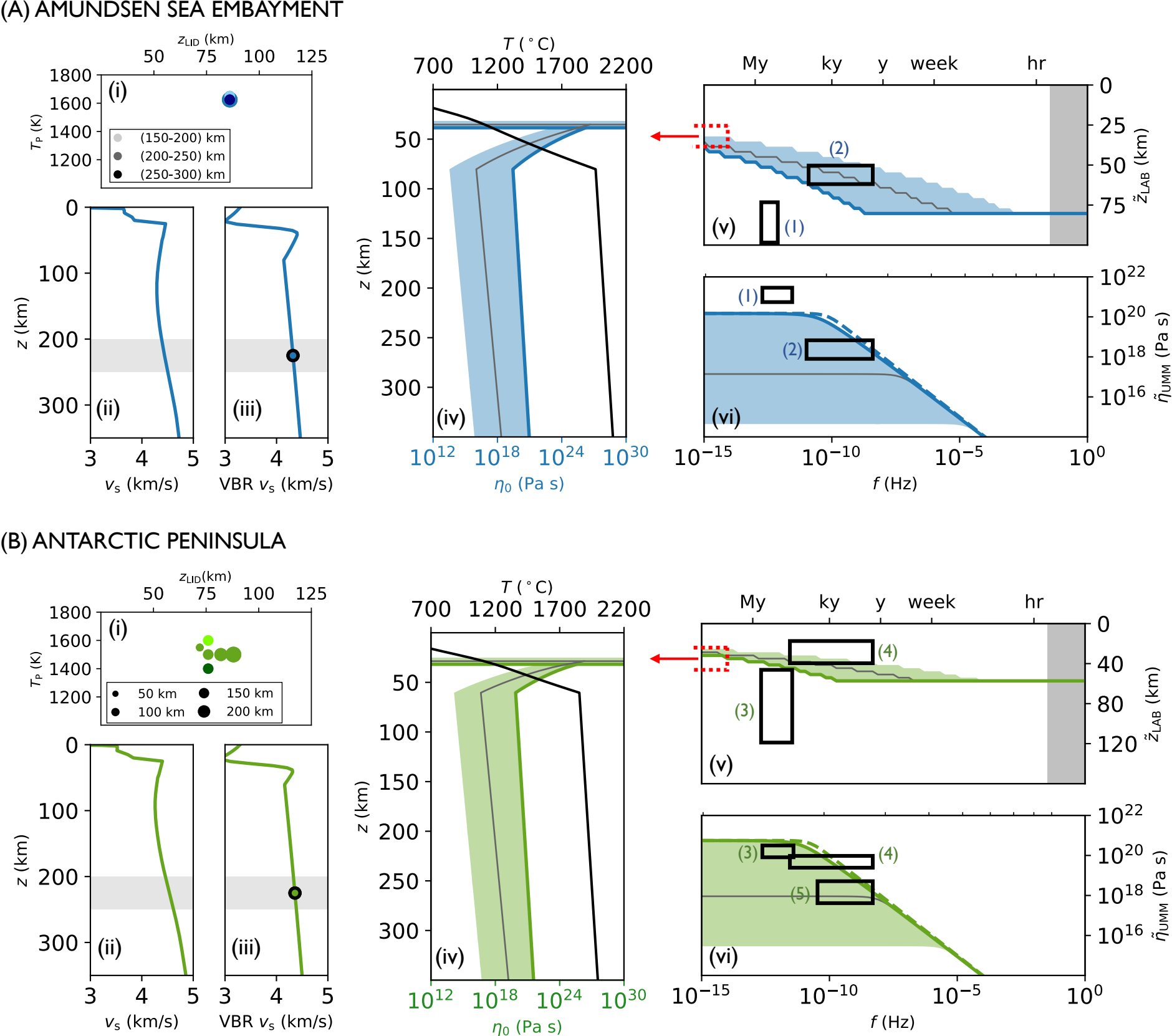
(A) AMUNDSEN SEA EMBAYMENT
z_{LID} (km)
50 75 100 125
1800 1600 1400 1200
T_P (K)
(i)
(150-200) km
(200-250) km
(250-300) km
0 100 200 300
z (km)
(ii)
(iii)
3 4 5
v_s (km/s)
VBR v_s (km/s)
T (°C)
700 1200 1700 2200
50 100 150 200 250 300
z (km)
(iv)
10^{12} 10^{18} 10^{24} 10^{30}
η_0 (Pa s)
My ky y week hr
0 25 50 75
$\tilde{z}_{LAB}$ (km)
(2)
(v)
(1)
10^{22} 10^{20} 10^{18} 10^{16}
$\tilde{\eta}_{UMM}$ (Pa s)
(1)
(2)
(vi)
10^{-15} 10^{-10} 10^{-5} 10^{0}
f (Hz)
(B) ANTARCTIC PENINSULA
z_{LID}(km)
50 75 100 125
1800 1600 1400 1200
T_P (K)
(i)
50 km
100 km
150 km
200 km
0 100 200 300
z (km)
(ii)
(iii)
3 4 5
v_s (km/s)
VBR v_s (km/s)
T (°C)
700 1200 1700 2200
50 100 150 200 250 300
z (km)
(iv)
10^{12} 10^{18} 10^{24} 10^{30}
η_0 (Pa s)
My ky y week hr
0 40 80 120
$\tilde{z}_{LAB}$ (km)
(4)
(3)
(v)
10^{22} 10^{20} 10^{18} 10^{16}
$\tilde{\eta}_{UMM}$ (Pa s)
(3)
(4)
(5)
(vi)
10^{-15} 10^{-10} 10^{-5} 10^{0}
f (Hz)

Figure 7.

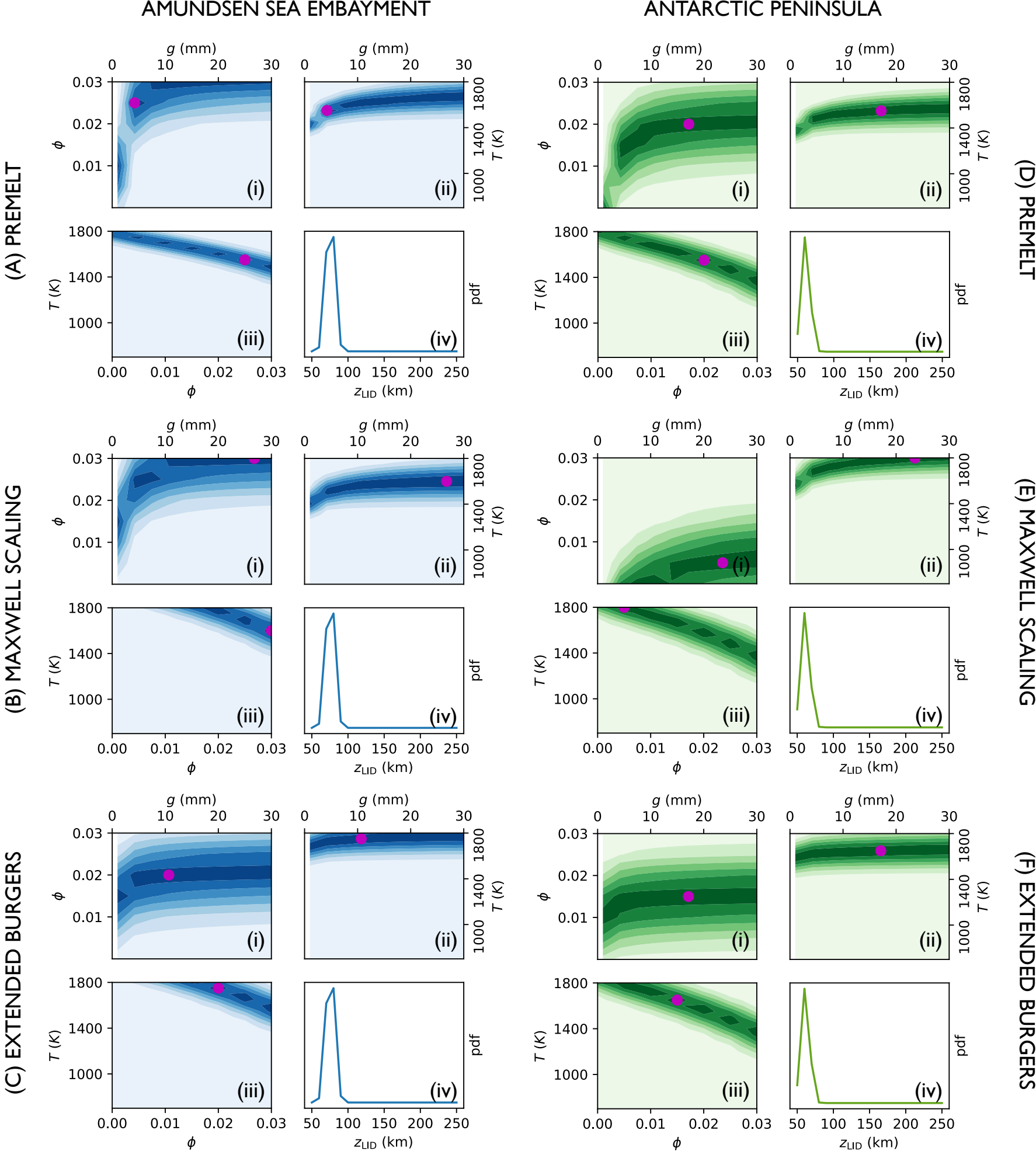
AMUNDSEN SEA EMBAYMENT
ANTARCTIC PENINSULA
(A) PREMELT
(B) MAXWELL SCALING
(C) EXTENDED BURGERS
(D) PREMELT
(E) MAXWELL SCALING
(F) EXTENDED BURGERS
g (mm)
ϕ
T (K)
pdf
z_{LID} (km)
(i)
(ii)
(iii)
(iv)

Figure 8.

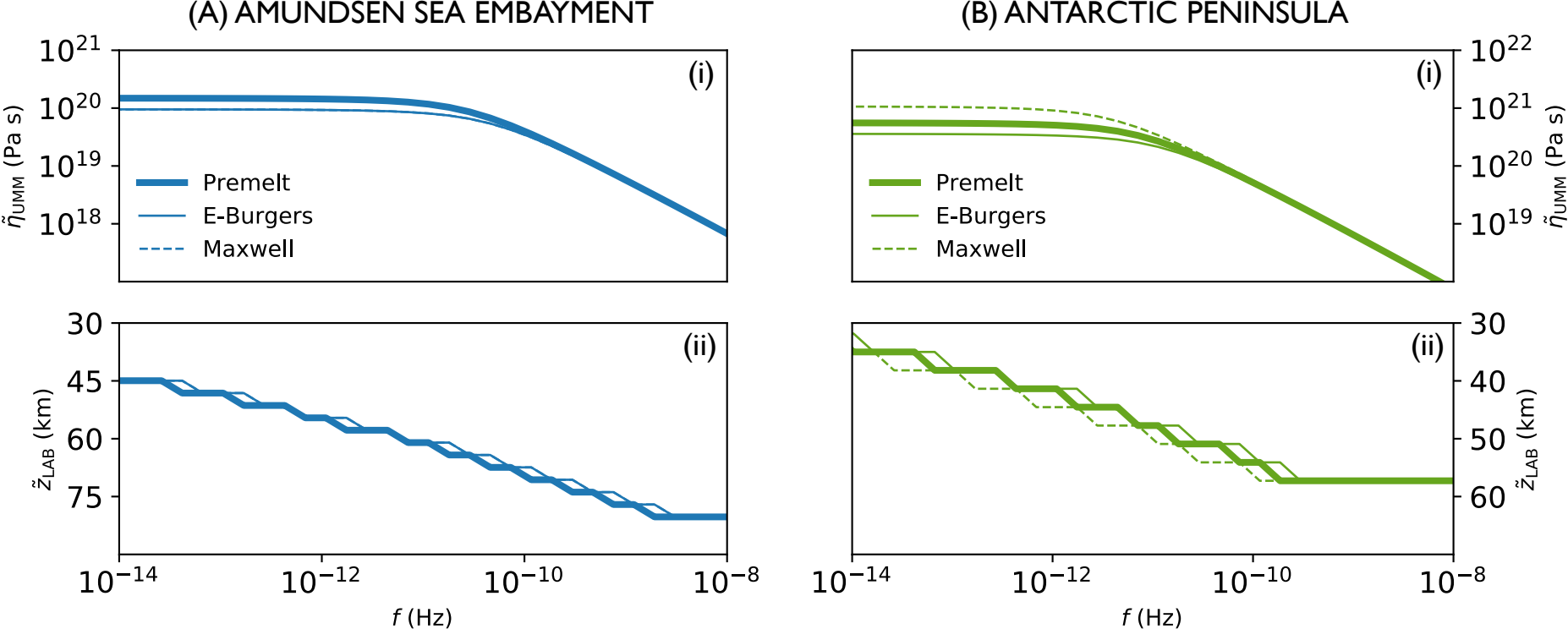
(A) AMUNDSEN SEA EMBAYMENT
(B) ANTARCTIC PENINSULA
(i)
(ii)
Premelt
E-Burgers
Maxwell
$\tilde{\eta}_{UMM}$ (Pa s)
$\tilde{z}_{LAB}$ (km)
f (Hz)
10^{21}
10^{20}
10^{19}
10^{18}
10^{22}
30
45
60
75
40
50
10^{-14}
10^{-12}
10^{-10}
10^{-8}

Figure A1.

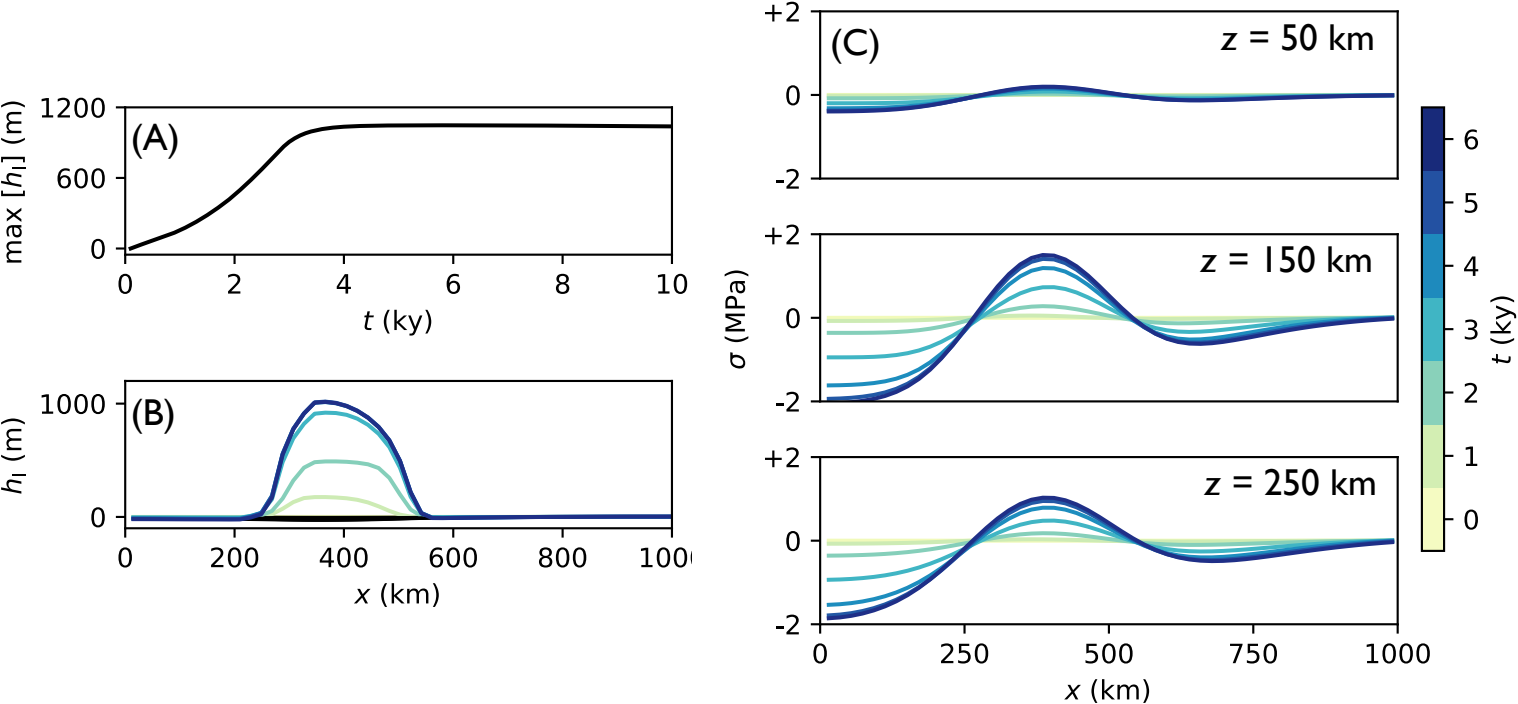
(A)
max [h_l] (m)
1200
600
0
0
2
4
6
8
10
t (ky)
(B)
h_l (m)
1000
0
0
200
400
600
800
1000
x (km)
(C)
z = 50 km
z = 150 km
z = 250 km
σ (MPa)
+2
0
-2
0
250
500
750
1000
x (km)
t (ky)
0
1
2
3
4
5
6